FAR-INFRARED AND SUBMILLIMETER EMISSION FROM GALACTIC AND EXTRAGALACTIC PHOTODISSOCIATION REGIONS

MICHAEL J. KAUFMAN

Department of Physics, San Jose State University, San Jose, CA 95192-0106, and Space Sciences Division, NASA Ames Research Center

MARK G. WOLFIRE

Department of Astronomy, University of Maryland, College Park, MD 20742

DAVID J. HOLLENBACH

Space Sciences Division, MS 245-3, NASA Ames Research Center, Moffett Field, CA 94035

AND

MICHAEL L. LUHMAN[1]

Naval Research Laboratory, Remote Sensing Division, Code 7217, Washington, DC 20375

ABSTRACT

Photodissociation region (PDR) models are computed over a wide range of physical conditions, from those appropriate to giant molecular clouds illuminated by the interstellar radiation field to the conditions experienced by circumstellar disks very close to hot massive stars. These models use the most up-to-date values of atomic and molecular data, the most current chemical rate coefficients, and the newest grain photoelectric heating rates, which include treatments of small grains and large molecules. In addition, we examine the effects of metallicity and cloud extinction on the predicted line intensities. Results are presented for PDR models with densities over the range $n = 10^1$–10^7 cm^{-3} and for incident far-ultraviolet radiation fields over the range $G_0 = 10^{-0.5}$–$10^{6.5}$ (where G_0 is the far-ultravioliet [FUV] flux in units of the local interstellar value), for metallicities $Z = 1$ and 0.1 times the local Galactic value, and for a range of PDR cloud sizes. We present line strength and/or line ratio plots for a variety of useful PDR diagnostics: [C II] 158 μm, [O I] 63 μm and 145 μm, [C I] 370 μm and 609 μm, CO $J = 1$–0, $J = 2$–1, $J = 3$–2, $J = 6$–5, and $J = 15$–14, as well as the strength of the far-infrared continuum. These plots will be useful for the interpretation of Galactic and extragalactic far-infrared and submillimeter spectra observable with the *Infrared Space Observatory* (*ISO*), the Stratospheric Observatory for Infrared Astronomy, the *Submillimeter Wave Astronomy Satellite*, the *Far Infrared and Submillimeter Telescope*, and other orbital and suborbital platforms. As examples, we apply our results to *ISO* and ground-based observations of M82, NGC 278, and the Large Magellanic Cloud. Our comparison of the conditions in M82 and NGC 278 show that both the gas density and FUV flux are enhanced in the starburst nucleus of M82 compared with those in the normal spiral NGC 278. We model the high [C II]/CO ratio observed in the 30 Doradus region of the LMC and find that it can be explained either by lowering the average extinction through molecular clouds or by enhancing the density contrast between the atomic layers of PDRs and the CO-emitting cloud cores. The ratio $L[\text{CO}]/M[\text{H}_2]$ implied by the low extinction model gives cloud masses too high for gravitational stability. We therefore rule out low-extinction clouds as an explanation for the high [C II]/CO ratio and instead appeal to density contrast in $A_V = 10$ clouds.

Subject headings: galaxies: ISM — infrared: ISM: lines and bands — infrared: ISM: continuum — ISM: atoms — ISM: molecules — submillimeter

1. INTRODUCTION

In the past two decades, infrared, submillimeter, and millimeter observations of Galactic molecular clouds illuminated by ultraviolet radiation from nearby stars have revealed strong far-infrared (FIR) grain continuum emission as well as moderately strong emission from warm gas in the fine-structure lines of [C II] 158 μm, [O I] 63 μm and 145 μm, [Si II] 35 μm, and [C I] 370 and 609 μm, as well as from low-J transitions of CO. A series of models have been used to interpret these observations (e.g., Tielens & Hollenbach 1985a, hereafter TH85; van Dishoeck & Black 1986, 1988a, 1988b; Sternberg & Dalgarno 1989; Wolfire, Tielens, & Hollenbach 1990, hereafter WTH90; Hollenbach, Takahashi, & Tielens 1991, hereafter HTT91; Abgrall et al. 1992; Le Bourlot et al. 1993; Köster et al. 1994; Sternberg &

Dalgarno 1995; Draine & Bertoldi 1996; Luhman et al. 1997b; Pak et al. 1998). Observations of Galactic sources are reviewed in Hollenbach & Tielens (1997, 1999). TH85 argued that the observed fine-structure line to dust-continuum flux ratios required a mechanism that was moderately efficient ($\sim$0.1%–1%) at converting far-ultraviolet (FUV) flux into atomic and molecular gaseous line emission. They showed that this condition is satisfied by grain photoelectric heating in the regions where FUV radiation from hot stars impinged on opaque molecular clouds. TH85 dubbed regions where the FUV radiation played a significant role in the heating and/or the chemistry "photodissociation regions" (PDRs), and they showed that the emission from such regions could be primarily parameterized by the cloud density, n, and the strength of the FUV (6 eV $< hv <$ 13.6 eV) radiation field, G_0, illuminating the cloud (where G_0 is in units of the Habing Field, 1.6×10^{-3} ergs cm^{-2} s^{-1}). In particular, WTH90 showed

that far-infrared observations of PDRs would be extremely useful in determining the physical properties of these regions.

PDRs are the origin of much of the infrared radiation from the interstellar medium (ISM). The incident starlight is absorbed by dust grains and large carbon molecules (polycyclic aromatic hydrocarbons [PAHs]) and reradiated primarily as PAH infrared features and infrared continuum radiation. As much as 0.1%-1% of the absorbed starlight, however, is converted to gas heating via photoelectric ejection of electrons from grains. The gas generally attains a higher temperature than the grains because of the much less efficient cooling of the gas (often via [C II] 158 μm and [O I] 63 μm emission) relative to the radiative dust continuum cooling, and inefficient coupling between gas and grains means that the gas and grains remain at different temperatures. Much of the [C II] and [Si II] and most of the [O I], [C I], and CO rotational emission from the Milky Way Galaxy arises from PDRs.

PDRs include all the neutral gas in the ISM, where FUV photons dominate a significant aspect of the chemistry and/or heating. Traditionally, PDRs have been associated with atomic gas. However, with the above definition, PDRs also include material in which the hydrogen is molecular and the carbon is mostly in CO, but in which FUV flux still strongly affects the chemistry of oxygen and carbon not locked in CO (photodissociating OH, O_2 and H_2O, for example) and affects the ionization fraction as well. The transition from H to H_2 and from C^+ to CO occurs in PDRs. With the exception of the molecular gas in dense, star-forming cores, most molecular gas in the Galaxy is found at $A_V \lesssim 5$ in giant molecular clouds where FUV radiation still plays an important role (Wolfire, Hollenbach, & Tielens 1993). Therefore, neutral diffuse clouds ($A_V < 1$), translucent clouds ($A_V \sim 1$), and 90% of molecular clouds ($A_V > 1$) are PDR gas—thus, most of the ISM is in PDRs.

In addition, the warm neutral medium ($n \simeq 0.25$ cm^{-3}) of the Galaxy (see McKee & Ostriker 1977; Wolfire et al. 1995), the neutral gas around planetary nebulae, and photodissociated winds from red giant or asymptotic giant branch (AGB) stars are PDRs. Densities in PDRs range from $n = 0.25$ cm^{-3} to $n \gtrsim 10^7$ cm^{-3}, and incident FUV fluxes range from $G_0 \lesssim 1$ (the interstellar radiation field) to $G_0 \gtrsim 10^6$ (the field $\lesssim 0.1$ pc from an O star). We treat the range 10 cm$^{-3} \leq n \leq 10^7$ cm^{-3} and $0.3 \leq G_0 \leq 3 \times 10^6$ in this paper. Comparison of observations with our models not only provide a diagnostic of n, T, and G_0 from the emitting regions but also constrain the metallicity, the geometry, the dust properties, and (for regions smaller than the beam) the cloud or clump properties such as the size, the volume and area filling factors, and the number of clouds or clumps in the beam.

As in Galactic sources, observations of PDRs in external galaxies show that the fine-structure lines of [C II] and [O I] generally dominate the global gas cooling (e.g., Stacey et al. 1991; Madden et al. 1993; Carral et al. 1994; Poglitsch et al. 1995), but [C I] and CO emission lines from well-shielded PDR gas can also contribute significantly (e.g., Büttgenbach et al. 1992; White et al. 1994; Stutzki et al. 1997). The measured strengths of especially the [C II] and [O I] lines and the FIR continuum, when compared to PDR models, can provide effective diagnostics of the typical conditions in extragalactic interstellar media (e.g., WTH90; Carral et al. 1994). In galaxies, however, the derived physical parameters are uncertain to the extent that media other than opaque PDRs can contribute to the line emission. For example, shock-heated media may contribute significantly to the [O I] 63 μm emission (Draine, Roberge, & Dalgarno 1983; Hollenbach & McKee 1989), as observed in the starburst galaxy NGC 6240 (Luhman et al. 1997a). Likewise, the extended low-density cold neutral component of the ISM (which is a nonopaque or diffuse PDR) may dominate the large-scale [C II] 158 μm emission, as suggested by Madden et al. (1993) for the galaxy NGC 6946. Furthermore, diffuse H II regions may dominate the production of [Si II] or [C II] in some galaxies (Lord et al. 1996a, 1996b).

New and upcoming infrared and submillimeter airborne and space-based platforms and sensitive detectors/receivers are greatly enhancing the sensitivity of extragalactic PDR observations. As a result, the number and variety of observed extragalactic PDRs continue to grow, posing increasingly more complicated challenges to theoretical PDR models. For instance, recent [C II] and [O I] FIR spectra of normal (Lord et al. 1996a, 1996b; Malhotra et al. 1997) and starburst (Fischer et al. 1996; Satyapal et al. 1999) galaxies obtained with the *Infrared Space Observatory* (*ISO*) reveal PDR gas that is generally typical of that found in other Galactic and extragalactic PDRs, where the ratio of [C II] to FIR flux is $\sim (1–3) \times 10^{-3}$ (Stacey et al. 1991). However, for some sources such as ultraluminous infrared galaxies (Luhman et al. 1998; Fischer et al. 1999, in preparation) and a few normal galaxies (Malhotra et al. 1997), *ISO* data indicate extremely low [C II]/FIR ratios $\sim(1–5) \times 10^{-4}$. Such low ratios may indicate that the sources of the grain heating are not OB stars but objects that radiate considerable bolometric luminosity in bands outside the FUV, or these ratios may indicate unusually high ratios of G_0 to n, which result in a dramatic decrease in the grain photoelectric heating of the gas because of the increase of positive grain charge (see § 3). Conversely, in dwarf irregular galaxies, [C II]/FIR is much higher than in the Galaxy (e.g., [C II]/FIR $\sim 1\%$ in the Large Magellanic Cloud; Poglitsch et al. 1995; Israel et al. 1996; Pak et al. 1998), perhaps because of the lower metallicities and lower dust-to-gas ratios. The paucity of dust that characterizes low-metallicity galaxies increases the penetration depth of photodissociating UV photons and produces clouds with reduced-size CO cores surrounded by larger PDRs, as evidenced by high ratios of [C II] to CO (Poglitsch et al. 1995; Israel et al. 1996; Madden et al. 1997). Likewise, recent sensitive Antarctic Submillimeter Telescope remote observer (AST/RO) observations of [C I] in the LMC show that the extent of [C I] emission, created by the photodissociation of CO, is also enhanced (Stark et al. 1997). We note that such metal-deficient galaxies are not good candidates for the standard conversion of CO intensity to H_2 mass (Maloney & Black 1988; Sakamoto 1996). Several authors have constructed PDR models appropriate to the Magellanic Clouds, with particular emphasis on the C^+/C/CO transition (Maloney & Black 1988; van Dishoeck & Black 1988a, 1988b; Lequeux et al. 1994; Maloney & Wolfire 1997; Pak et al. 1998). These studies demonstrate that, in order to match the observed PDR line emission from metal-deficient systems such as the Magellanic Clouds, low-abundance models specific to the environment are required.

WTH90 presented especially useful contour plots of the fine-structure emission and line ratios predicted by their

PDR models as a function of G_0 and n. Several recent developments motivate us to update the calculations presented by WTH90. From a theoretical standpoint, many of the important physical parameters that effect the calculation of emissions from PDRs (e.g., collision strengths, chemical rate coefficients, photoelectric heating rates) have been revised in recent years, in some cases by orders of magnitude, so we might expect the predictions of these models to change considerably. We extend the work of WTH90 to include a larger parameter space for n and G_0, and to include a study of the effects of changing the metallicity and geometry. We also include results for a wider variety of predicted diagnostic lines (e.g., [C I] and CO). From an observational standpoint, results from recent, existing, and future observatories will be used to study Galactic and extragalactic PDRs in greater detail than ever before. These include the *Infrared Space Observatory* (*ISO*); the Stratospheric Observatory for Infrared Astronomy (SOFIA; NASA's planned successor to the Kuiper Airborne Observatory [KAO]), which will be used to study far-infrared sources with unprecedented spectral and spatial resolution; the *Submillimeter Wave Astronomy Satellite* (*SWAS*) and the Odin telescope, which will be used to observe the sky in submillimeter transitions of CI, O_2, H_2O and CO; and the *Far Infrared and Submillimeter Telescope* (*FIRST*), which will be used to study a wide range of Galactic and extragalactic phenomena over a broad spectral range.

The outline of this paper is as follows. In § 2 we discuss the relevant details of our PDR model. We concentrate on the important differences between our present calculations and previous studies by our group. Recent observational work has led us to select a new set of atomic abundances, while recent theoretical work has led to improvements in our understanding of several important reaction and heating rates, and we discuss these and other important differences.

In § 3 we present a series of contour plots of line strengths and line ratios of important atomic and molecular cooling species. We divide an opaque PDR into a warmer surface region ($A_V \lesssim 2$) and a cooler, more molecular interior ($A_V \sim 1$–5). In §§ 3.1 and 3.2 we focus on emission from the surface regions and present surface temperatures as well as line strengths and line ratios of several important far-infrared cooling lines, including the [C II] 158 μm line and the [O I] 63 μm and 145 μm lines. We also compare the strengths of these transitions with the integrated far-infrared continuum intensity expected from PDRs. This line-to-continuum ratio provides a measure of the efficiency with which stellar photons are converted to gas heating in PDRs. In § 3.3 we concentrate on the interior part of the PDR, where longer wavelength tracers, the neutral carbon transitions at 609 μm and 370 μm and several millimeter and submillimeter transitions of carbon monoxide, originate.

In § 4, we discuss how changes in the assumed metallicity and in the model geometry can affect our results. We briefly describe our procedure (WTH90) for deriving the average physical parameters of an ensemble of PDRs when large beams are used to study distant (e.g., extragalactic) interstellar media. Our procedure for applying our results to ensembles of clouds is relevant for the interpretation of the far-infrared, millimeter and submillimeter observations of, for instance, the nuclei of starburst galaxies that exhibit metallicities close to solar, as well as the Magellanic Clouds

or other irregular galaxies that show reduced metallicities. These results are applied to the starburst galaxy M82, the normal spiral galaxy NGC 278, and the Large Magellanic Cloud.

2. PDR MODELS

The basis for our new modeling effort is the PDR model of TH85 and HTT91, which computes a simultaneous solution for the chemistry, radiative transfer, and thermal balance in PDRs. Assuming gas-phase elemental abundances and grain properties, each model is essentially described by a constant density of H nuclei, n, throughout the PDR and the intensity of the far-ultraviolet radiation field at the PDR surface, G_0.

These models have been used in the past to show how the structure of a molecular cloud varies with increasing optical depth. TH85 and HTT91 described the general morphology of the surface layers for typical ratios $G_0/n \gtrsim 10^{-2}$ cm^3, as is often the case: an outer layer ($A_V \sim 1$) of atomic H, C$^+$ and O, a central layer where the H makes the transition to H_2 ($A_V \sim 1$–2) and where C$^+$ becomes C and then CO ($A_V \sim 2$–4), and an inner layer ($A_V \sim 3$–10) where the oxygen not incorporated into CO is still mainly in atomic O. At larger depths, we leave the PDR and enter the very opaque molecular cores where the chemistry and heating are dominated by cosmic rays.

2.1. The Standard Model

We list here the standard input parameters for the model results presented in the contour plots of the following section. The input parameters are the microturbulent velocity dispersion of the gas, δv_D; the gas-phase elemental abundances; the dust abundances, including those of polycyclic aromatic hydrocarbons (PAHs), which generally dominate the grain-photoelectric heating; the gas density, n; and the strength of the incident FUV field, G_0.

Our model clouds are assumed to be pressure supported with a microturbulent Doppler line width of $\delta v_D = 1.5$ km s^{-1}; this value of the line width is taken from observational studies of fine-structure and CO line widths (e.g., Hollenbach & Tielens 1999) and is appropriate for the majority of cases that we consider. This value of δv_D is low for cases of high G_0 and high for cases of low G_0, but variation of this parameter by factors of $\lesssim 2$ has little effect on the calculated line strengths (Wolfire, Hollenbach, & Tielens 1989). We use the cool diffuse cloud gas-phase abundances from Savage & Sembach (1996) for our standard model. In § 4, we discuss the effects of changes in these gas-phase abundances. We assume the same grain FUV absorption characteristics as used in TH85 and HTT91, but we modify the grain photoelectric heating rates and the formation rate of H_2 on grains, as described below. With these parameters fixed, our study covers the range 10 cm$^{-3} \le n \le 10^7$ cm^{-3} and $10^{-0.5} \le G_0 \le 10^{6.5}$. Table 1 summarizes the standard input parameters.

Besides changing the standard gas-phase abundances (note in particular the decrease in the gas-phase carbon abundance in Table 1 from the value used in WTH90), we have made a number of changes to the chemical, heating, and cooling rate coefficients as compared with TH85, WTH90, and HTT91. We use revised collision rates as discussed in Burton, Hollenbach, & Tielens (1990), Spaans et al. (1994), and Wolfire et al. (1995). These include rates for

TABLE 1

STANDARD MODEL PARAMETERS

Parameter	Symbol	Value
Turbulent Doppler velocity (km s^{-1})...........	δv_D	1.5
Carbon abundance[a]	x_C	1.4×10^{-4}
Oxygen abundance[a]	x_O	3.0×10^{-4}
Silicon abundance[a]	x_{Si}	1.7×10^{-6}
Sulfur abundance[a]	x_S	2.8×10^{-5}
Iron abundance[a]	x_{Fe}	1.7×10^{-7}
Magnesium abundance[a].........................	x_{Mg}	1.1×10^{-6}
Dust abundance relative to diffuse ISM	δ_d	1
FUV dust absorption/visual extinction	δ_{UV}	1.8
Dust visual cross section per H (cm^2)	σ_V	5×10^{-22}
Formation rate of H$_2$ on dust[b] (cm^3 s^{-1})......	R_{form}	3×10^{-17}
PAH abundance	$x_{PAH} = n_{PAH}/n$	4×10^{-7}
Cloud density (cm^{-3})............................	n	$10^1 \leq n \leq 10^7$
Incident FUV flux	G_0	$10^{-0.5} \leq G_0 \leq 10^{6.5}$

[a] Gas-phase abundances relative to H nuclei from Savage & Sembach 1996.
[b] Rate per unit volume given by $R_{form} n_{H I} n$.

the collisional excitation of H$_2$ by impacts with H, H$_2$, and e^- (using modified rates from Draine et al. 1983 and Hollenbach & McKee 1979 as discussed in Burton et al. 1990), the excitation of O I by impacts with H^0, e^-, and H$^+$ (Péquignot 1990), the impacts of C II with e^- (Blum & Pradhan 1992), and C and O collision rates with H$_2$ (Schröder et al. 1991; Jaquet et al. 1992). The ortho- and para-H$_2$ fractions needed for the collision rates are calculated as in Burton, Hollenbach, & Tielens (1992).

We use the grain photoelectric heating rate as derived by Bakes & Tielens (1994). This rate includes a size distribution of particles extending from large grains (~ 0.25 μm) to small (~ 5 Å) PAHs and explicitly accounts for the microphysics of small particles. We use the "flat" PAH geometry as discussed in their paper and a grain size distribution proportional to $a^{-3.5}$ (the so-called MRN distribution; Mathis, Rumpl, & Nordsieck 1977), which extends to the PAH domain. The total PAH abundance n_{PAH}/n is approximately 4.0×10^{-7} with this assumption. Also included is the Bakes & Tielens (1994) cooling term due to electron recombinations onto positively charged grains. Vibrational heating by FUV-pumped H$_2$ as well as the vibrationally excited H$_2$ (H$_2^*$) abundances and H$_2$ rotational level populations are calculated using the prescription given in Burton et al. (1990). The dust temperature, important for gas heating at large optical depths, is found using the formulae in HTT91, and the gas-grain heat exchange is calculated as in Hollenbach & McKee (1989).

The gas-phase chemical reaction rates have been updated according to the list of Millar, Farquhar, & Willacy (1997; UMIST Database). We have incorporated PAH chemistry using PAH$^-$, PAH^0, and PAH$^+$ species and have included photoionization and electron recombination onto PAHs, charge exchange between metal ions and PAH^0, and metal ion recombination with PAH$^-$. The chemical rates are calculated using the equations in Bakes & Tielens (1994) and Draine & Sutin (1987). We have also modified the cosmic-ray heating and ionization terms using fits to the results of Shull & Van Steenberg (1985; see Wolfire et al. 1995 for functions). We have retained most of the photodissociation rates from Wolfire et al. (1990), with a few notable exceptions. The rate for OH photodissociation is taken from the Millar et al. (1997) list. The photodissociation rate of O$_2$

and the photoionization rate of Mg are taken from Spaans et al. (1994) for the $T_{eff} = 30,000$ K case, appropriate for the interstellar FUV radiation field. Abgrall et al. (1992) reevaluated the dissociation rate of H$_2$ in the interstellar medium. Their rate for an unshielded H$_2$ molecule in the radiation field of the local ISM amounts to $R_{photo} = 4.7 \times 10^{-11}$ s^{-1}, and we have adopted this rate. The photodissociation of CO is calculated as in Burton et al. (1990) except for the CO shielding factor, which is taken from van Dishoeck & Black (1988a). This factor includes both H$_2$ shielding and CO self-shielding.

Previously, we and others have used relatively complex expressions (Hollenbach & McKee 1979, 1989) for the rate coefficient of H$_2$ formation on grain surfaces. This rate coefficient depends sensitively on the H atom collision rate with grains, the sticking coefficient (itself a function of the grain temperature and the thermal velocity of the H atoms), and the probability of an absorbed atom producing an H$_2$ molecule before evaporating. While the collision frequency increases with the gas temperature, the sticking coefficient and H$_2$ formation efficiency decrease with temperature. In light of the realistic uncertainties in the H$_2$ formation rate, we have simplified our former treatment. Here we adopt the observationally derived (cf. Jura 1974) formation rate coefficient of $R_{form} = 3 \times 10^{-17}$ cm^3 s^{-1}. The formation rate per unit volume is then given by $R_{form} n_{H I} n$. We find that the resultant formation rate coupled with the photodissociation rate of Abgrall et al. (1992) closely matches the observed molecular fraction as a function of total hydrogen column density as seen in the diffuse interstellar medium (e.g., Dixon, Hurwitz, & Bowyer 1998).

We find that the most significant differences in the [C II] and [O I] line intensities from those reported in Wolfire et al. (1990) result from the new heating term that now includes the important effects of PAH heating. At high densities and FUV fields, the modified O I collision rates are also partly responsible for the differences. We also find that PAH chemistry can affect the depth of the C$^+$/C/CO transition with PAHs drawing the transition closer to the PDR surface (see Bakes & Tielens 1998 for a discussion of the effects of PAHs on the chemistry of PDRs). Neglecting PAH chemistry can lead to underestimates in the [C I] line intensities by a factor of 2.

3. RESULTS

In this section, we show our results for the strengths and line ratios of various cooling lines, as well as the continuum emission from grains, over the complete parameter space for our standard model (cf. Table 1). We present contour plots over the range 10 cm$^{-3} \leq n \leq 10^7$ cm^{-3} and $10^{-0.5} \leq G_0 \leq 10^{6.5}$. We begin by presenting contours of the PDR surface temperature as a function of G_0 and n (§ 3.1). In § 3.2, we give results for the strengths of the important far-infrared lines [C II] 158 μm, [O I] 63 μm and 145 μm, and the far-infrared continuum; in § 3.3, we present the strengths of the millimeter and submillimeter transitions [C I] 370 μm and 609 μm, CO $J = 1-0$, $J = 2-1$, $J = 3-2$, $J = 6-5$, and the far-infrared CO $J = 15-14$ transition. Table 2 lists these 10 important PDR cooling transitions, their wavelengths, upper energy levels E_{upper}, and critical densities n_{cr}.

3.1. Thermal Balance and the PDR Temperature

Unlike Wolfire et al. (1990), who found in many cases a significant initial rise in gas temperature with cloud depth, we find that the inclusion of PAH heating leads to a relatively constant PDR gas temperature from the cloud surface to a depth where either the heating or cooling changes significantly and the temperature drops. The heating is generally dominated by the grain photoelectric effect, and this changes primarily when dust attenuation significantly lowers the FUV flux, at $\tau_{\mathrm{FUV}} > 1$ or a column density $N \gtrsim 10^{21}$ cm^{-2}. Collisional deexcitation of FUV-pumped H_2 can dominate the heating in cases of high $G_0 \gtrsim 10^3$ and high $n \sim 10^5$–10^6 cm^{-3}. The cooling changes when the primarily atomic (H, C$^+$ and O) surface becomes molecular (H_2 or CO) at depths of $N \gtrsim 3 \times 10^{21}$ cm^{-2} for $G_0/n \gtrsim 3 \times 10^{-3}$ cm^3 (such that dust shields the molecules from dissociating radiation) or at smaller column densities for $G_0/n \lesssim 3 \times 10^{-3}$ cm^3 (such that self-shielding by H_2 and CO becomes dominant).

Figure 1 shows the PDR surface temperature, T_S, as a function of G_0 and n. In general, T_S rises with G_0 as would be expected since grain photoelectric heating dominates and the FUV flux is the source of the heating. There is an exception to this rule for very high fluxes, $G_0 \sim 10^6$, and very low gas densities [$n \lesssim 10^2$ cm^{-3}], where the grains become so positively charged because of the FUV flux that

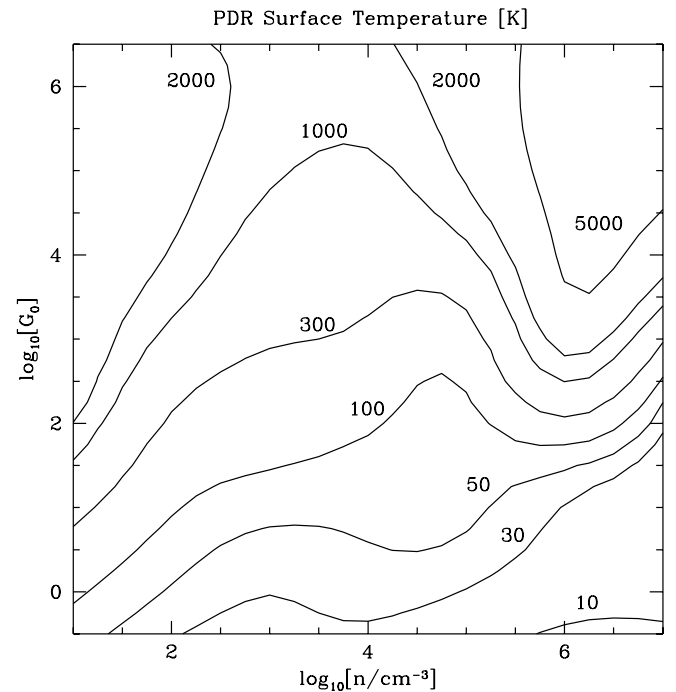FIG. 1.—Surface temperature of the atomic gas as a function of n and G_0. Contour levels are in kelvins.

increasing G_0 actually decreases the net heating. This heating drop stems from the poor heating efficiency of ejecting electrons from positively charged dust grains and increased rate of recombination cooling with the grains. However, as we discuss below, the results in this corner of parameter space are not realistic since the model does not take into account grain drift through the gas due to radiation pressure, which becomes important in this region. Fortunately, there are not many astrophysical regions that correspond to the upper left quadrant of our G_0-n parameter space.

The behavior of T_S with density is somewhat more complicated. At low densities ($n \lesssim 10^4$–10^5 cm^{-3}), the temperature drops for increasing n at fixed G_0. This behavior arises because the cooling is generally dominated by the [C II] 158 μm and [O I] 63 μm transitions whose critical densities lie at n_{cr}(C II) $\simeq 3 \times 10^3$ cm^{-3} and n_{cr}(O I) $\simeq 5 \times 10^5$ cm^{-3}, respectively. Thus the cooling rate per unit volume increases with n^2 in the low-density regime, whereas the grain photoelectric heating increases with a lower density dependence. The heating has, at least, an n^1 dependence since the grain density is proportional to n. In addition, as the gas-phase electron density increases, the grains become less positively charged. The diminished charge leads to a larger fraction of photoelectrons that escape the grains and increases the kinetic energy that they supply to the gas. The total density dependence for grain heating, however, is less than the n^2 dependence of cooling. At moderate densities ($n \sim 10^4$–10^6 cm^{-3}), [O I] and [C II] attain LTE, the cooling rate per unit volume is proportional to n, and the heating rate increases faster than the cooling rate. Here, T_S increases with increasing n at fixed G_0. Because the interstellar cooling curve is relatively flat as a function of T for 300 K < T < 3000 K (Dalgarno & McCray 1972), the temperature rapidly rises with n in this regime ($G_0 \gtrsim 10^4$) to thousands of degrees, at which coolants such as [O I] $\lambda 6300$ can become important and balance the heating. Finally, at

TABLE 2
PDR DIAGNOSTIC TRANSITIONS

Species	Transition	Wavelength (μm)	E_{upper}/k (K)	n_{cr}[a] (cm^{-3})
[C II]......	$^2P_{3/2} - {}^2P_{1/2}$	157.74	92	3×10^3
[O I]	$^3P_1 - {}^3P_2$	63.18	228	5×10^5
[O I]	$^3P_0 - {}^3P_1$	145.53	326	1×10^5
[C I]	$^3P_1 - {}^3P_0$	609.14	23.6	5×10^2
[C I]	$^3P_2 - {}^3P_1$	369.87	62.5	3×10^3
CO	$J = 1-0$	2600.78	5.53	3×10^3
CO	$J = 2-1$	1300.39	16.59	1×10^4
CO	$J = 3-2$	867.00	33.19	5×10^4
CO	$J = 6-5$	433.56	116.16	4×10^5
CO	$J = 15-14$	173.62	663.36	8×10^6

[a] Critical density for [C II], [O I], and [C I] for collisions with H. Critical density for CO for collisions with H_2. Critical densities for atoms ([C II], [O I], and [C I]) from TH85. Critical densities for CO calculated from $n_{\mathrm{cr}} = A_{ul}/\gamma_{ul}$ for a temperature of 100 K, A-values from Rothman et al. 1987, and values of γ_{ul} from Viscuso & Chernoff 1988.

very high densities ($n \gtrsim 10^6$ cm^{-3}), and especially for $G_0 \lesssim 10^4$, the temperature again declines with n. Here the grains have become neutral so that the heating rate per unit volume due to grains is just proportional to n (or the grain density), whereas the cooling increases somewhat more rapidly with n because of the presence of additional coolants such as [O I] $\lambda 6300$ and gas collisions with cold dust grains, whose efficiencies go as n^2, in addition to the LTE coolants [O I] 63 μm and [C II] 158 μm, whose efficiencies go as n.

3.2. [C II] 158 μm, [O I] 63 μm and 145 μm, and the Far-Infrared Continuum

In this section we present results for the strengths of several important far-infrared tracers of photodissociation regions. The emission is produced primarily in the outer regions of the UV-illuminated clouds, where H$_2$ and CO are photodissociated and cooling is dominated by neutral species and by singly ionized species whose ionization potentials are less than 13.6 eV. It is this outer region where the temperature contour plot (Fig. 1) applies and where the PDR line cooling occurs through the [C II] and [O I] transitions.

In Figure 2, we show schematically the various regimes that determine the relative strengths of the principal coolants of PDRs: the [C II] 158 μm transition and the [O I] 63

Important PDR Regimes
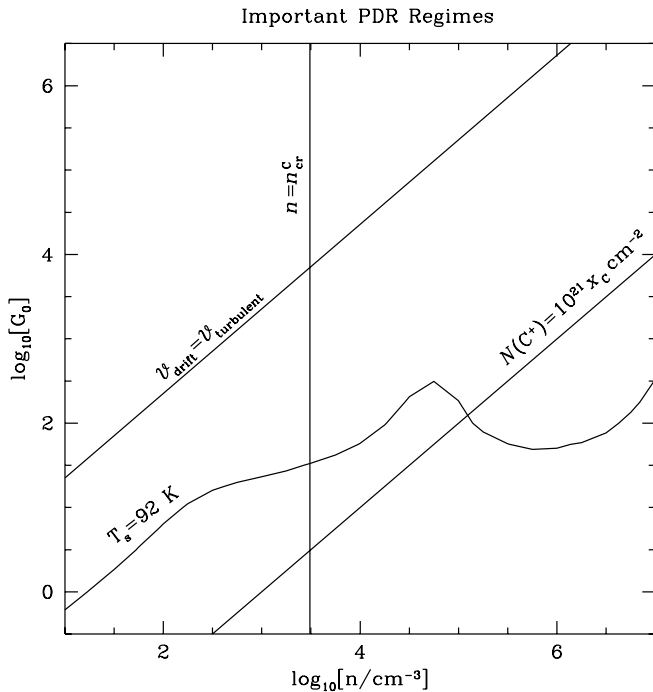
FIG. 2.—Important regimes for determining the intensity of a cooling line in a PDR. The line $n = n_{cr}^C$ roughly marks the critical density for the [C II] 158 μm, CO $J = 1$–0, and [C I] 370 μm transitions. For optically thin lines at constant column density, line intensities increase $\propto n^1$ for $n < n_{cr}$ and $\propto n^0$ for $n > n_{cr}$. The line $v_{drift} = v_{turbulent}$ shows where radiation pressure causes grains to drift with a speed equal to the gas turbulent speed. Parameter space above this line is inconsistent with a steady state model. The curve $T_S = 92$ K shows where the surface gas temperature is equal to the [C II] energy level above ground ($kT_S = \Delta E$). Above this curve the [C II] intensity, for constant column density, is weakly dependent on G_0. The line $N(C^+) = 10^{21}x_C$ traces the location of a constant C^+ column density ($\sim 10^{17}$ cm^{-2}), equivalent to all carbon being singly ionized to a hydrogen column density of 10^{21} cm^{-2}. Below this line gas shielding of the FUV field becomes important and the C^+ column density and the [C II] line intensity become sensitive to G_0/n.

μm transition. Above the line marked "$v_{drift} = v_{turbulent}$," radiation pressure drives grains through the gas at velocities greater than the assumed average turbulent velocities ($\sim \delta v_D$) in the gas. The models are therefore inconsistent far above this line since the models assume no significant drifting of grains with respect to the gas and no significant gas heating or chemical effects due to the grain drift. The line marked $n = n_{cr}^C$ is roughly the critical density of [C II] 158 μm, CO $J = 1$–0 and [C I] 370 μm. To the left of this line, the line intensities of these species rise rapidly with n (linearly with n for optically thin transitions at constant column density and temperature). To the right of this line, the line intensities increase more slowly with n (as n^0 for constant column density and temperature as LTE is reached). The line marked $T_S = 92$ K marks the regions with surface temperatures of 92 K, the excitation temperature above ground of the [C II] 158 μm transition. Above this line, the PDR temperatures exceed 92 K and the [C II] 158 μm line intensity rises weakly with G_0, for a constant C^+ column. Below this line, the PDR temperature drops below 92 K and the [C II] 158 μm intensity is much more sensitive to G_0. The line marked $N(C^+) = 10^{21}x_C$ cm^{-2} indicates the boundary between a relatively constant column of C^+ and a falling column of C^+, where x_C is the fractional abundance of gas-phase carbon relative to H nuclei. Above and to the left of the line, the absorption of FUV flux is dominated by grain opacity, and the column density of C^+ is approximately constant, $\sim 10^{21}x_C$ cm^{-2}, corresponding to all carbon in C^+ in a hydrogen nucleus column density of 10^{21} cm^{-2}. Below and to the right of this line, H$_2$ and C opacity dominate the absorption of FUV flux and $N(C^+)$ drops significantly below $10^{21}x_C$ cm^{-2}. A hydrogen column density of 10^{21} cm^{-2} corresponds to an FUV opacity due to grains of order unity, so this line marks the boundary between dust shielding and gas (atomic carbon and H$_2$) shielding of the carbon-ionizing FUV flux. Below and to the right of this line, which occurs at $G_0/n \simeq 3 \times 10^{-3}$ cm^{-3}, the column density of C^+ is quite sensitive to the ratio G_0/n. One of the key reactions that enhances the shielding of the FUV by atomic carbon is the neutralization of C^+ by neutral and negatively charged PAHs. Above and to the left of this line, the column of C^+ is set by the grain opacity, which fixes the C^+ column at roughly $\sim 10^{21}x_C$ cm^{-2}. Therefore, above this line and in the region where $n > n_{cr}^C$ and $T > 92$ K, the [C II] 158 μm line intensity is mainly determined by the C^+ column, which is relatively insensitive to changes in n and G_0.

In calculating the temperature structure and line emission from PDRs, we have used the TH85 escape probability formalism for a one-dimensional semi-infinite slab. This formalism assumes that the IR line photons escape from only the front face of the slab, and their average intensity is the integrated escaping emissivity (or flux) divided by 2π. The approximation is quite good for [O I] 63 μm emission, which is optically thick in the PDR, but only marginally so for the [C II] 158 μm emission, which typically has line center optical depths of ~ 1. Therefore, the [C II] and [O I] line intensities plotted in the following figures are the emergent fluxes from one face of the PDR layer divided by 2π.

In Figure 3, we show the intensity of the important PDR cooling transition, [C II] 158 μm ($^2P_{3/2}$–$^2P_{1/2}$), as a function of n and G_0. The behavior may be understood by referring to Figure 2 and examining several distinct regions of the parameter space. The intensity of the [C II] line scales
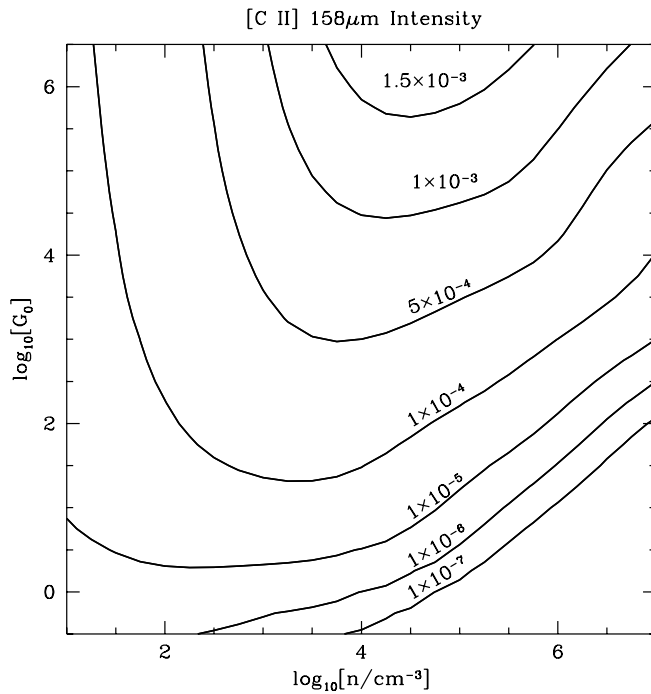
[C II] 158μm Intensity

FIG. 3.—[C II] 158 μm intensity emitted from the surface of a photodissociation region as a function of the cloud density, n, and the FUV flux incident on the cloud, G_0, for our standard model parameters. Contours are labeled with the line intensity in units of ergs cm^{-2} s^{-1} sr^{-1}.

approximately as $I(C\ II) \propto N(C^+)e^{(-92/T)}/[1 + (n_{cr}^C/n)]$, where $N(C^+)$ is the column density of ionized carbon, $\Delta E/k \sim 92$ K is the energy of the upper state of the 158 μm transition, and $n_{cr}^C \simeq 3 \times 10^3$ cm^{-3} is the critical density of the 158 μm transition. In the lower left portion of the figure, $T < 92$ K, $n < n_{cr}^C$, and $N(C^+) \sim 10^{21}x_C$ since dust dominates the absorption of carbon-ionizing photons. In this lower left region (roughly $G_0 \lesssim 10$, $n \lesssim 3 \times 10^3$ cm^{-3}), the column of C$^+$ is constant but the intensity of [C II] 158 μm emission rises very sharply with increasing G_0 because $T < 92$ K and T increases with G_0. On the other hand, for fixed G_0, the [C II] 158 μm intensity is not very sensitive to n. This is because T drops with increasing n (see § 3.1), which offsets the increasing collision rate (the n/n_{cr}^C term). More insight into this cancellation can be gained by noting that [C II] 158 μm emission dominates the cooling in this regime and that therefore the [C II] 158 μm intensity is proportional to the total heat input via grain photoelectric heating. In this regime, the grains are quite neutral and the column-integrated grain photoelectric heating is just proportional to G_0 and independent of n. Roughly 3% of the incident FUV flux is converted to [C II] 158 μm flux, with most of the rest emerging as grain IR continuum.

In the upper left region (roughly $G_0 \gtrsim 10$, $n \lesssim 3 \times 10^3$ cm^{-3}), the column of C$^+$ is constant and the intensity of [C II] 158 μm emission is nearly independent of G_0, since $T > 92$ K and increases in T do not appreciably change the intensity. On the other hand, the intensity now scales with n/n_{cr}^C.

In the upper right region of the plot, above the $N(C^+) \simeq 10^{21}x_C$ cm^{-2} line and for $n \gtrsim 3 \times 10^3$ cm^{-3}, the column of C$^+$ is constant, $T > 92$ K, and $n > n_{cr}^C$, so the intensity of [C II] 158 μm is fairly constant and only weakly dependent on G_0 and n (the intensity changes by ~ 10 as G_0 and n

vary by more than 10^3). In this region of parameter space, [O I] cooling is dominant.

In the lower right region of the plot, below the $N(C^+) \simeq 10^{21}x_C$ cm^{-2} line, $N(C^+)$ begins to drop significantly. The crucial reaction neutralizing C$^+$ is not electronic recombination, which is slow (rate coefficient of order 10^{-11} cm^3 s^{-1} with an electron abundance of order 10^{-4}), but the neutralization of C$^+$ by neutral and negatively charged PAHs (rate coefficients of order 10^{-8} to 10^{-6} cm^3 s^{-1} with an abundance of 4×10^{-7}). The neutral carbon reacts with various species including OH, H$_2^*$, and O in a set of reactions leading to CO (see Hollenbach & Tielens 1999, Fig. 9b.) The column of C$^+$ and the temperature are controlled by the ratio G_0/n, which is why lines of constant G_0/n have constant [C II] 158 μm intensity in this region.

For high values of G_0 (and hence high temperatures), the conditions become appropriate for strong [O I] 63 μm emission, which has a higher upper-state energy ($E_{upper}/k \sim 228$ K) than does [C II] 158 μm (92 K). Figure 4 shows the ratio of the intensity of the [O I] 63 μm ($^3P_1$–$^3P_2$) transition to that of the [C II] 158 μm transition. At high G_0 the PDR surface temperature is above the upper state energy for both [C II] and [O I], and the column of warm C$^+$ and O is set by dust attenuation of the FUV. The ratio [O I]/[C II] is therefore roughly constant for fixed n in this regime. However, at low G_0 or low T, the 63 μm intensity falls faster with decreasing G_0 than does the 158 μm intensity, and the ratio drops. The critical density of the [O I] 63 μm transition ($n_{cr}^O \sim 5 \times 10^5$ cm^{-3}) is considerably higher than that of the [C II] transition, so at densities greater than $\sim 3 \times 10^3$ cm^{-3} the 63 μm intensity continues to increase rapidly with density while the 158 μm intensity is relatively constant with increasing density; thus for $T \gg 100$ K (or $G_0 \gg 10$) and 3×10^3 cm$^{-3} < n < 5 \times 10^5$ cm^{-3}, the [O I] 63 μm to [C II] 158 μm intensity ratio climbs rapidly with n.

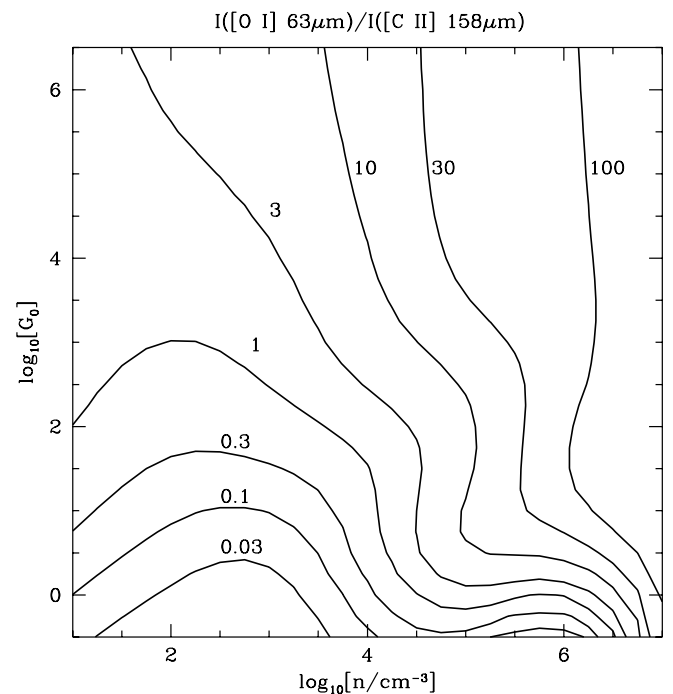I([O I] 63μm)/I([C II] 158μm)

FIG. 4.—Ratio of the intensity of the [O I] 63 μm line to the intensity of the [C II] 158 μm line emitted from the surface of a photodissociation region as a function of the cloud density, n, and the FUV flux incident on the cloud, G_0, for our standard model parameters.

Figure 5 shows contours of the [O I] 145 μm $(^3P_0-^3P_1)$/[O I] 63 μm $(^3P_1-^3P_2)$ intensity ratio as a function of G_0 and n. The [O I] 63 μm line is generally optically thick (line center optical depths of several) over our entire parameter space. The 145 μm line, by contrast, is optically thin over the entire parameter space. The ratio varies by less than an order of magnitude over nearly the entire range of G_0 and n. Both transitions have similar critical densities, so the ratio is relatively insensitive to density but does decrease somewhat for $n > 10^5$ cm^{-3}. Excitation of the 145 μm transition requires $\Delta E/k$ of $\sim$ 325 K, about 100 K higher than that of the 63 μm transition, so the ratio becomes more sensitive to temperature (or G_0) for $T \lesssim 300$ K or $G_0 \lesssim 10^2$.

Figure 6 shows the ratio of the sum of the strengths of the two major cooling lines, [O I] 63 μm and [C II] 158 μm, to the bolometric FIR dust continuum emission. Care must be taken when using this plot because the results depend both on the geometry and morphology of the observed region and on the fraction of dust heating that occurs outside the FUV band. As discussed above, we assume that IR line photons escape only from the front face of the PDR and that the intensity in a line is the integrated line flux divided by 2π. In contrast to the atomic line emission, the grains radiate optically thin FIR continuum radiation that escapes from the front and back of most interstellar clouds. Therefore if a finite slab is illuminated from one side by a flux G_0 and all grain heating is by FUV photons, the FIR continuum intensity radiated back is given by $I_{FIR} = 1.3 \times 10^{-4}G_0$ ergs cm^{-2} s^{-1} sr^{-1} (recall that $G_0 = 1$ corresponds to 1.6×10^{-3} ergs cm^{-2} s^{-1} and $1.3 \times 10^{-4} = 1.6 \times 10^{-3}/4\pi$). Typically for OB stars, however, there is about equal heating of the grains by photons outside the FUV band (TH85), so the observed intensity is roughly $I_{FIR} \simeq 2 \times (1.3 \times 10^{-4})G_0$ ergs cm^{-2} s^{-1} sr^{-1}. Figure 6 uses this approximation for the emergent infrared intensity.
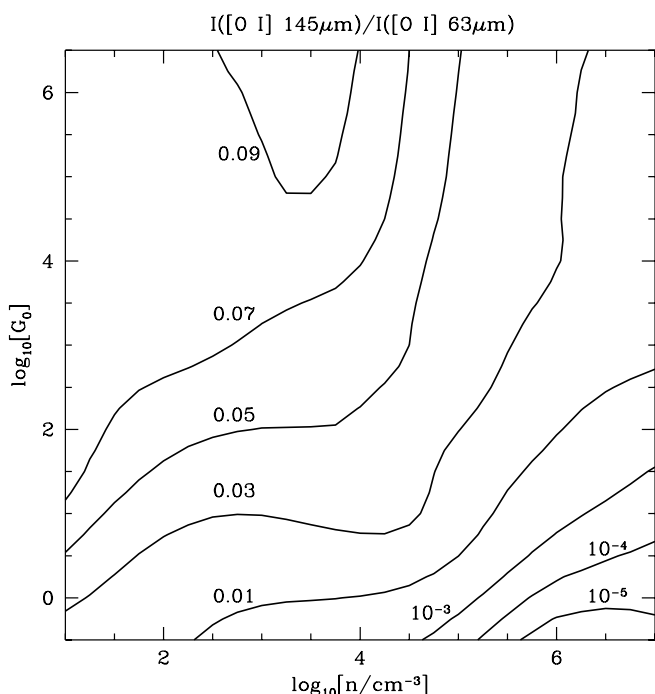
I([O I] 145μm)/I([O I] 63μm)

FIG. 5.—Ratio of the intensity of the [O I] 63 μm line to the [O I] 145 μm line as a function of the cloud density, n, and the FUV flux incident on the cloud, G_0, for our standard model parameters.
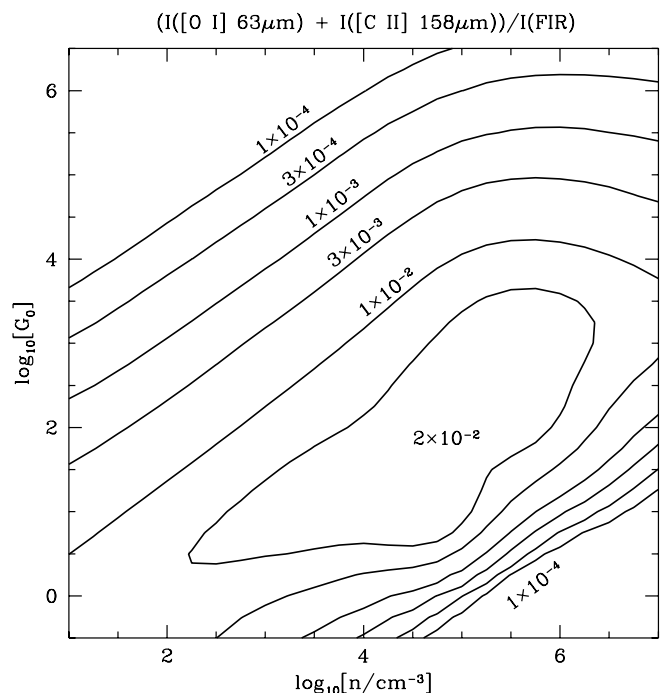
(I([O I] 63μm) + I([C II] 158μm))/I(FIR)

FIG. 6.—Ratio of the intensity of the [C II] 158 μm and [O I] 63 μm lines to the total far-infrared intensity emitted from the surface of a photodissociation region as a function of the cloud density, n, and the FUV flux incident on the cloud, G_0, for our standard model parameters. See text for cautions on using this figure.

For the case of clouds in the active regions of galaxies, or where many clouds are contained within the beam, another situation arises. Here the clouds are illuminated from all sides and the observer sees the optically thin FIR continuum from both the near and far side of the cloud, whereas the [O I] 63 μm emission (and to a lesser extent the [C II] 158 μm emission) is observed only from the side facing the observer. For clouds illuminated on all sides by G_0, the observed ([O I] 63 μm + [C II] 158 μm)/FIR ratio is simply the ratio of the escaping intensities of line photons to grain continuum for each cloud. This corresponds to $I([O I] 63 \mu$m + [C II] 158 μm)/$2I_{FIR}$, where $I_{FIR} \simeq 2 \times (1.3 \times 10^{-4})G_0$ ergs cm^{-2} s^{-1} sr^{-1} accounts for an approximate bolometric correction of 2, as before. Therefore, when modeling clouds illuminated on all sides, the contours of Figure 6 should be reduced by a factor of 2.

The contours of Figure 6 may be understood by analyzing the effect of G_0/n on photoelectric heating and on the depth to which C$^+$ and O exist in the PDR. For $G_0/n \gtrsim 3 \times 10^{-3}$ cm^3, C$^+$ and O exist to a depth of at least $\tau_{FUV} \gtrsim 1$, where τ_{FUV} is the FUV optical depth of the dust. Since [C II] 158 μm and [O I] 63 μm dominate the cooling when they are abundant, the emission by these species is just equal to the grain photoelectric heating of the gas. The grain photoelectric heating efficiency, ϵ, is defined as the ratio of the FUV energy that goes into the gas to the FUV energy that goes into grain heating (TH85). For $n \leq 10^5$ cm^{-3} and $G_0/n \gtrsim 10^{-2}$ cm^3, the contours track this efficiency and are given by roughly $\frac{1}{2}\epsilon$ where the factor of $\frac{1}{2}$ arises because of the bolometric correction. Note that the constant contour lines track constant ratios G_0/n since this ratio controls the grain positive charge, which, in turn, controls the gas heating. The relationship breaks down in the upper right

quadrant of the figure, where $G_0 \gtrsim 10^4$ and $n \gtrsim 10^5$ cm^{-3}, since the PDR temperature is high ($T \gtrsim 5000$ K) and the " recombination cooling" of the gas caused by electrons recombining on grains becomes significant. In other words, the energy of the recombining electrons becomes comparable to the energy of the photoejected electrons, and the gas heating is significantly reduced.

For $G_0/n \lesssim 3 \times 10^{-3}$ cm^3, the C$^+$/C/CO transition is drawn to the cloud surface. In this regime, much of the grain photoelectric heating of the gas emerges as [C I] or CO line emission, so the ([O I] 63 μm + [C II] 158 μm)/FIR ratio is reduced below $\frac{1}{2}\epsilon$.

3.3. [C I] 370 μm and 609 μm and CO Rotational Lines

In this section we present results for the strengths of lines that are generally produced in gas deeper within PDRs, where ionization of carbon gives way to neutral carbon (C^0) and carbon monoxide (CO). These lines lie at millimeter and submillimeter wavelengths and dominate the cooling at moderate depths in PDRs. For high $G_0/n \gtrsim 10^{-3}$, these species exist at depths of $A_V \sim 2$–10. In these PDRs most of the FUV heating of the gas occurs at $A_V \lesssim 1$ and the CO and [C I] lines are generally weaker than [C II] and [O I]. However, for low values of $G_0/n \lesssim 3 \times 10^{-3}$, gas shielding allows C and CO to dominate the cooling at small column densities into the cloud, and the [C I] and mid-J CO intensities exceed those of [C II] and [O I]. The [C I] and mid-J CO lines are therefore useful for determining the details of the chemistry and penetration of the incident FUV in PDRs.

In Figure 7, we show the [C I] 609 μm ($^3P_1$–$^3P_0$) intensity, as a function of n and G_0. As discussed in TH85, Tielens & Hollenbach (1985b), and HTT91, the column density of neutral carbon is insensitive to the strength of the external FUV field. Only the depth at which the C$^+$/C/CO transition occurs depends on the FUV field (see TH85 for details). The intensity of [C I] 609 μm emission increases slightly with density up to $n_{\rm cr}^{\rm C I\,609} \sim 5 \times 10^2$ cm^{-3}, reflecting the greater collisional excitation with n for $n < n_{\rm cr}$ but then slowly decreases with increasing density, reflecting a smaller column of C with increasing density. Neutral C is mainly destroyed by FUV ionization and is formed by electron recombination with C$^+$, neutralization of C$^+$ by negatively charged PAHs, and FUV photodissociation of carbon-containing molecules. At high densities, neutral carbon may be formed by FUV photodissociation of CH$_2$ and CH$_3$, and the reaction H + CH $\rightarrow$ C + H$_2$; at lower densities, the photodissociation of CH and CH$_2$ also contributes to the abundance of C since these molecules cannot quickly react with O to form CO. Note that the entire dynamic range of the line intensity is less than a factor of 20 over most of our G_0/n parameter space.

Figure 8 shows the ratio of the two submillimeter neutral carbon transitions, [C I] 370 μm/[C I] 609 μm. Both transitions have relatively low upper-state energies ($E_{609}/k \sim 24$ K, $E_{370}/k \sim 63$ K). Therefore, the ratio has a very weak temperature dependence in most of the parameter space since T is generally $\gtrsim 50$ K in the [C I]-emitting region. In addition, the critical densities of the two transitions are similar ($n_{\rm cr}^{\rm C I\,609} \sim 3 \times 10^2$ cm^{-3}, $n_{\rm cr}^{\rm C I\,370} \sim 2 \times 10^3$ cm^{-3}). Since emission in both lines is from the same species, the ratio is unaffected by the abundance of neutral carbon. The figure clearly shows that the ratio is insensitive to the strength of the radiation field as long as the temperature is large enough to excite both transitions; only in the high n, low G_0 region is temperature a factor since this combination leads to low temperatures at the C$^+$/C/CO transition. Below the critical densities, the intensity ratio varies
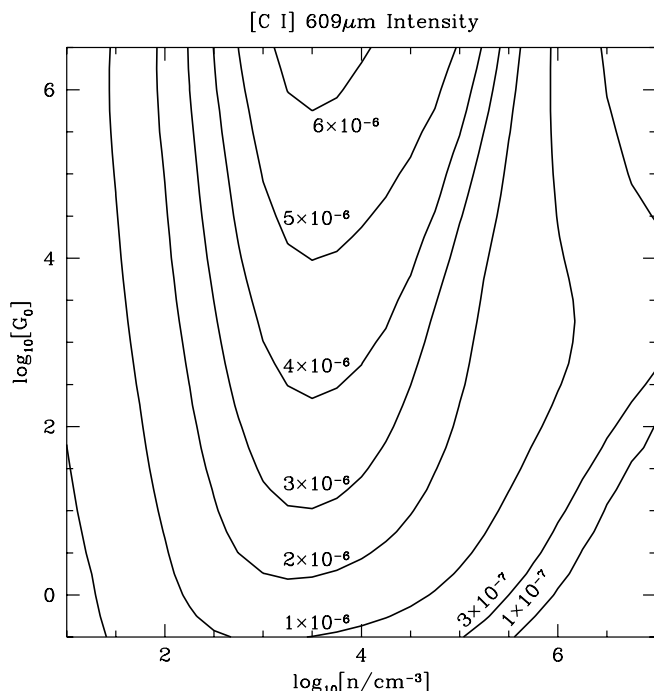

FIG. 7.—[C I] 609 μm intensity emitted from the surface of a photodissociation region as a function of the cloud density, n, and the FUV flux incident on the cloud, G_0, for our standard model parameters. Contours are labeled with the line intensity in units of ergs cm^{-2} s^{-1} sr^{-1}.
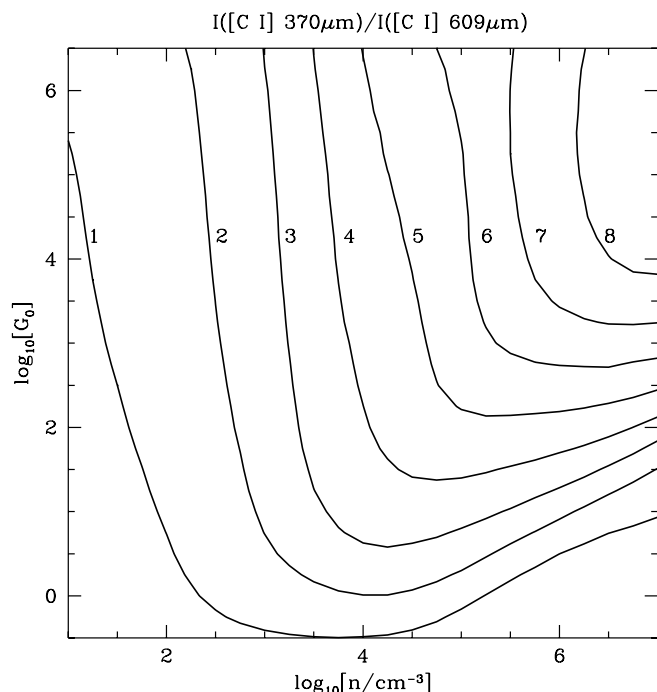

FIG. 8.—Ratio of the intensity of the [C I] 370 μm line to the [C I] 609 μm line as a function of the cloud density, n, and the FUV flux incident on the cloud, G_0, for our standard model parameters.

by a factor of 2 in 1 order of magnitude in density, while above the critical densities it takes nearly 3 orders of magnitude in density to change the intensity ratio by a factor of 2.

Figure 9 shows the ratio of intensities in the [C II] 158 μm and the CO $J = 1$–0 transitions. Note that our PDR model assumes that the cloud is sufficiently thick ($A_V > 4$) that a C^+ to CO transition front exists in the cloud. Both transitions have similar critical densities (cf. Table 2). The CO $J = 1$–0 line rapidly becomes optically thick once C^+ converts to CO. As discussed in Wolfire et al. (1993), the CO $J = 1$–0 intensity is very insensitive to G_0 because the temperature of the CO $J = 1$–0 "photosphere" is very insensitive to G_0. Typically, $T_{CO} \sim 10$–50 K for $G_0 \sim 1$–10^5. Only at very small ratios of G_0/n does T drop below 10 K at the $C^+/C/CO$ transition so that the $e^{-5.5 K/T}$ term in the collision rate becomes important and the level populations become subthermal. (Note that Fig. 1 shows the surface temperature and not the temperature of the $C^+/C/CO$ transition.) The [C II] 158 μm/CO $J = 1$–0 ratio is largely determined by the column density of C^+ and T_S, which drop (see Fig. 2) as gas shielding begins to dominate. As mentioned above, the C^+ column density is roughly set by the ratio G_0/n for $G_0/n < 3 \times 10^{-3}$ cm^3, and thus the decrease in the intensity ratio seen in the lower right portion of the figure is dominated by the drop in the C^+ column. In addition, the ratio drops slightly for decreasing G_0 as the temperature of the [C II]–emitting gas drops below 92 K. Note that over a large part of G_0/n parameter space, corresponding to ratios $G_0/n \simeq 10^{-3}$ to 1 cm^3, the [C II]/CO intensity ratio is 10^3–10^4, a value often observed in Galactic PDRs (Stacey et al. 1991).

Figure 10 shows the ratio of intensities in the [C I] 609 μm and the CO $J = 1$–0 transitions. The behavior is similar
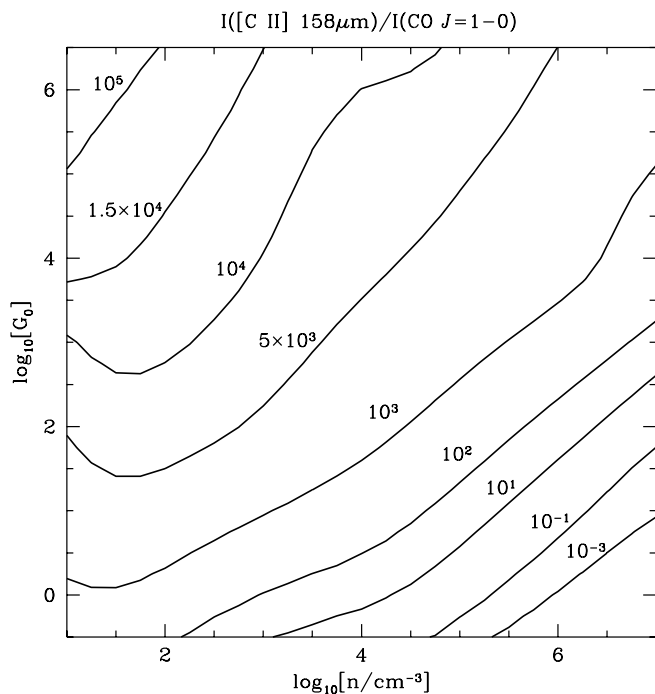

$I([\text{C I}]\ 609\mu\text{m})/I(\text{CO}\ J = 1 - 0)$

FIG. 10.—Ratio of the intensity of the [C I] 609 μm line to the CO $J = 1$–0 2.6 mm line as a function of the cloud density, n, and the FUV flux incident on the cloud, G_0, for our standard model parameters, with assumptions noted in § 3.3.
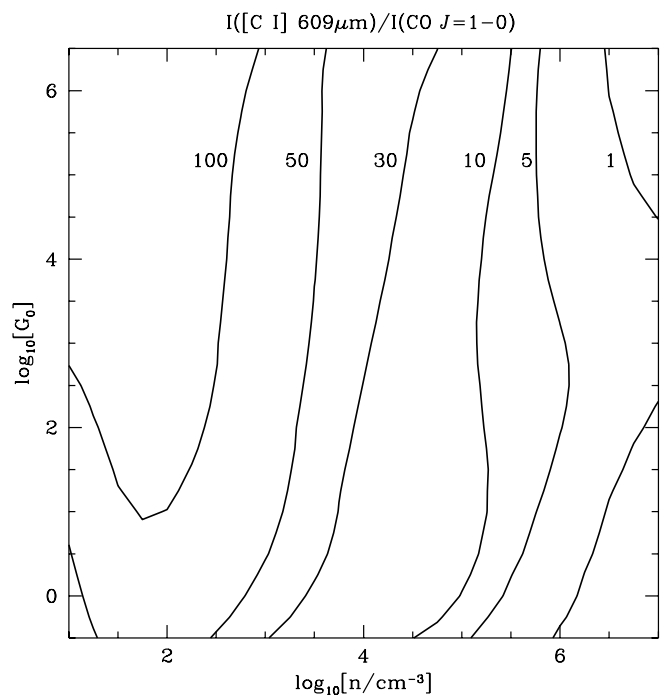

$I([\text{C II}]\ 158\mu\text{m})/I(\text{CO}\ J = 1 - 0)$

FIG. 9.—Ratio of the intensity of the [C II] 158 μm line to the CO $J = 1$–0 2.6 mm line as a function of the cloud density, n, and the FUV flux incident on the cloud, G_0, for our standard model parameters, with assumptions noted in § 3.3.

to that in the previous figure. For densities below $n_{cr} \sim 10^3$ cm^{-3}, both transitions increase in strength with increasing n. However, CO increases faster with n than [C I], so the [C I]/CO ratio drops with n; for [C I] the increase in collisional excitation is somewhat offset by a decrease in [C I] column, as described above. Above $n_{cr}^{CO\ J=1-0}$, the [C I] strength decreases as the column density decreases with n. The CO intensity meanwhile is approximately constant for $n > 10^4$ cm^{-3}, so the intensity ratio falls.

Figure 11 shows the intensity of the CO $J = 1$–0 2.6 mm transition as a function of G_0 and n. For densities below the critical density ($n_{cr}^{CO\ J=1-0} \sim 5 \times 10^3$ cm^{-3}), the line intensity increases roughly linearly with n; above the critical density, the line intensity changes far more slowly. Since this line is generally optically thick, the intensity is mainly sensitive to the temperature at the surface of the $C^+/C/CO$ transition region, especially for $n > n_{cr}^{CO\ J=1-0}$. Since the upper state energy lies only 5.5 K above ground, the temperature sensitivity increases for very low values of T_{CO}; this may be seen in the lower right-hand side of the figure where the intensity is sensitive to increases in G_0. Again it should be emphasized that the temperature, T_{CO}, at which CO goes optically thick is an extremely weak function of G_0. Often this temperature is roughly the grain temperature at the $C^+/C/CO$ boundary. The grain temperature varies as $G_0^{0.2}$ at the cloud surface but has an even weaker dependence on G_0 at the $C^+/C/CO$ boundary since the boundary moves to greater depths as G_0 increases.

Figure 12 shows the CO $J = 2$–$1/J = 1$–0 intensity ratio. In general, both lines are optically thick in PDRs, and the $J = 2$–1 line becomes optically thick closer to the PDR surface (i.e., at higher T than the $J = 1$–0 line). The ratio is only weakly dependent on gas density over most of the
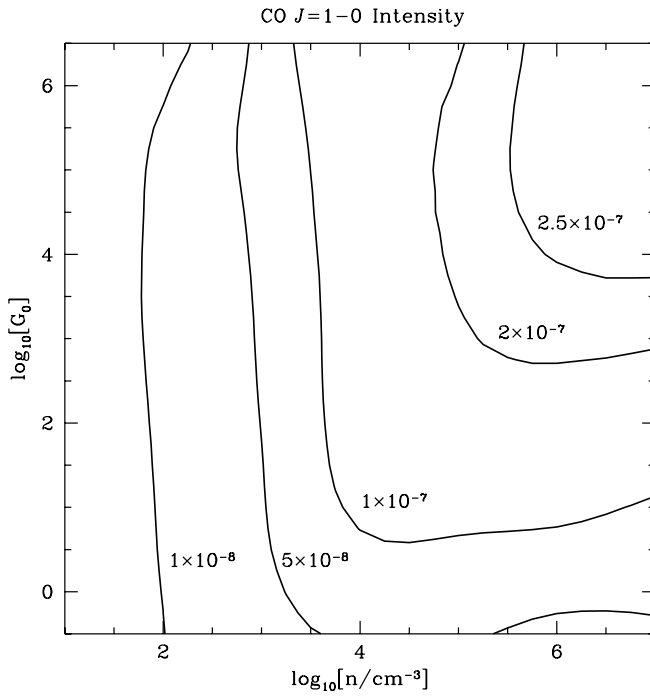
CO $J=1-0$ Intensity

FIG. 11.—CO $J = 1-0$ 2.6 mm intensity emitted from the surface of a photodissociation region as a function of the cloud density, n, and the FUV flux incident on the cloud, G_0, for our standard model parameters. Contours are labeled with the line intensity in units of ergs cm^{-2} s^{-1} sr^{-1}.

parameter space. Both transitions have similar critical densities (see Table 2) and the intensity ratio increases only slightly with n above this value. For very low values of G_0/n the temperature at the C$^+$/C/CO transition falls below the
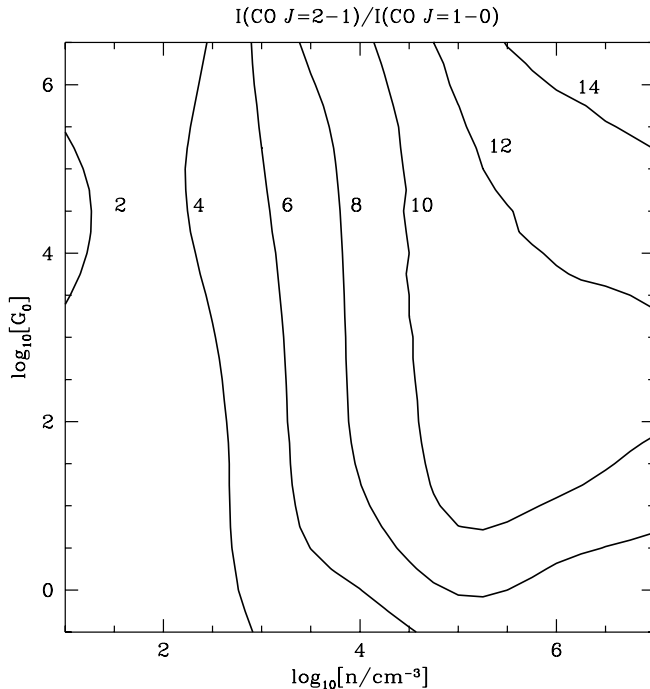
$I(CO\ J=2-1)/I(CO\ J=1-0)$

FIG. 12.—Ratio of the intensity of the CO $J = 2-1$ 1.3 mm line to the CO $J = 1-0$ 2.6 mm line as a function of the cloud density, n, and the FUV flux incident on the cloud, G_0, for our standard model parameters. Contours may be converted to antenna temperature ratios by multiplying by 0.125, with assumptions noted in text.

energy of the $J = 2-1$ transition upper state and the ratio drops. The intensity ratio in Figure 12 may be converted to an integrated antenna temperature ratio, $\int T_A(2-1)dv/ \int T_A(1-0)dv$, by multiplying by 0.125; this conversion is valid if one assumes that both transitions have the same intrinsic line width and fill the same fraction of the beam. The behavior of the contours in Figure 12 can also be seen in Figures 13, 14, and 15, where the ratio of the $J = 3-2$, $J = 6-5$, and $J = 15-14$ intensities to that of the $J = 1-0$ transition are plotted (the intensity ratio in Fig. 13 can be converted to an antenna temperature ratio by multiplying by 0.037). All of these figures show the same behavior as that seen in Figure 12, except that the critical densities become increasingly larger so that the density dependence of the ratio is strongest for the highest J transitions. In addition, at $n \ll n_{cr}$, the relative intensities reflect the collisional excitation rates out of the $J = 0$ ground state. As J_{upper} increases, the rates get progressively smaller relative to the rate to $J_{upper} = 1$. Note particularly that in Figure 15 the $J = 15-14$ transition never gets nearly as strong as the $J = 1-0$ transition except at very high densities, $n \sim 10^{5.5}$ cm^{-3}. For this line, which lies ~ 600 K above ground, there is both a temperature and density sensitivity that makes the $J = 15-14/J = 1-0$ ratio extremely high in the upper right quadrant of the figure. The strength of the $J = 15-14$ transition drops so rapidly below and to the left of the plotted contours that the ratio of the two lines falls to $\lesssim 10^{-4}$ as either the temperature or density fall; note that the strength of the $J = 1-0$ line is relatively constant over the entire parameter space, varying by only ~ 25 over the full range of n and G_0 (see Fig. 11).

3.4. Effects of Varying Metallicity, A_V, and Cloud Geometry

As noted in the introduction, many galaxies show evidence for low metallicity, and the Milky Way Galaxy has significant metallicity gradients, so we are motivated to explore the effects of lowered gas-phase abundances and lowered dust fractions on the results of our models. In addition, we study the effect of varying the total column density or A_V through an irradiated cloud. We explore results for both planar and spherical PDR clouds with reduced gas metallicity and dust fractions.

In this section, we focus on emission from two PDR diagnostics: the [C II] 158 μm transition, which is emitted primarily from the warm atomic regions at $A_V \lesssim 1$, and the CO $J = 1-0$ transition, which is generally emitted from cooler molecular regions at $A_V \gtrsim 2$. We chose these two transitions since they are bright emission lines and are readily seen in a wide variety of sources (e.g., Stacey et al. 1991). Comparable resolution observations ($\sim 1'$) in both transitions have existed for several years for Galactic sources, normal and starburst galaxies, and low-metallicity galaxies. Our results show that the ratio of the two transitions is sensitive to the total PDR visual extinction, since CO line emission comes from higher A_V. This effect can be exaggerated in spherical PDR models where the volume of [C II]–emitting gas may be much larger than that of the CO-emitting gas. Lowering the metallicity enhances this effect for clouds of fixed hydrogen column, N.

3.4.1. Effects of Varying Metallicity and A_V

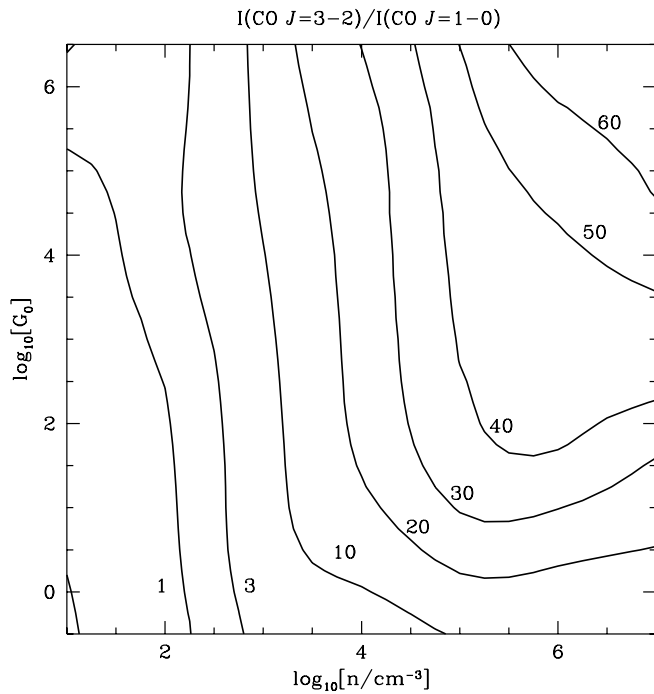For our planar PDR models, we have studied our entire n-G_0 parameter space with metallicities down to $Z = 0.1$.

I(CO $J=3-2$)/I(CO $J=1-0$)

I(CO $J=15-14$)/I(CO $J=1-0$)

FIG. 13.—Ratio of the intensity of the CO $J = 3$–2 867 μm line to the CO $J = 1$–0 2.6 mm line as a function of the cloud density, n, and the FUV flux incident on the cloud, G_0, for our standard model parameters. Contours may be converted to antenna temperature ratios by multiplying by 0.037, with assumptions noted in text.

FIG. 15.—Ratio of the intensity of the CO $J = 15$–14 173.6 μm line to the CO $J = 1$–0 2.6 mm line as a function of the cloud density, n, and the FUV flux incident on the cloud, G_0, for our standard model parameters.

We take a reduced metallicity to correspond to a reduction in both the gas-phase heavy-element abundance and the dust abundance. Therefore, a metallicity $Z = 0.1$ corresponds to all of the gas-phase abundances in Table 1 falling
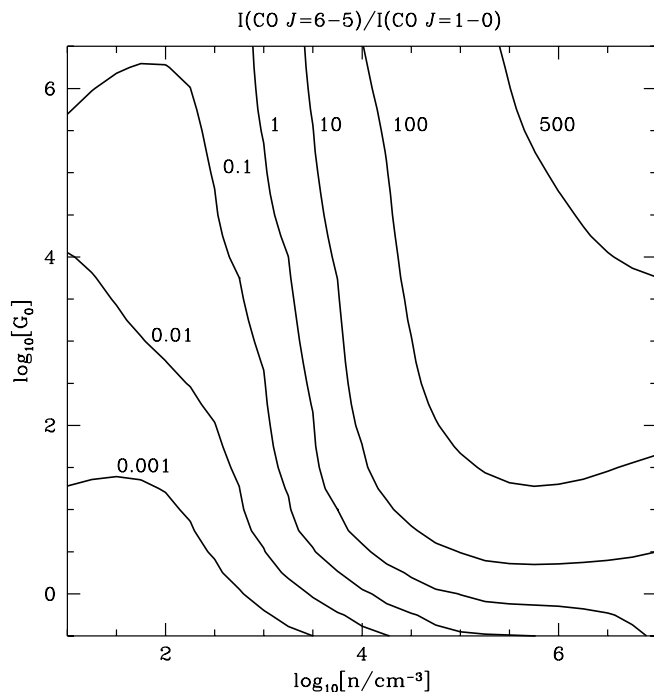
I(CO $J=6-5$)/I(CO $J=1-0$)

FIG. 14.—Ratio of the intensity of the CO $J = 6$–5 433 μm line to the CO $J = 1$–0 2.6 mm line as a function of the cloud density, n, and the FUV flux incident on the cloud, G_0, for our standard model parameters.
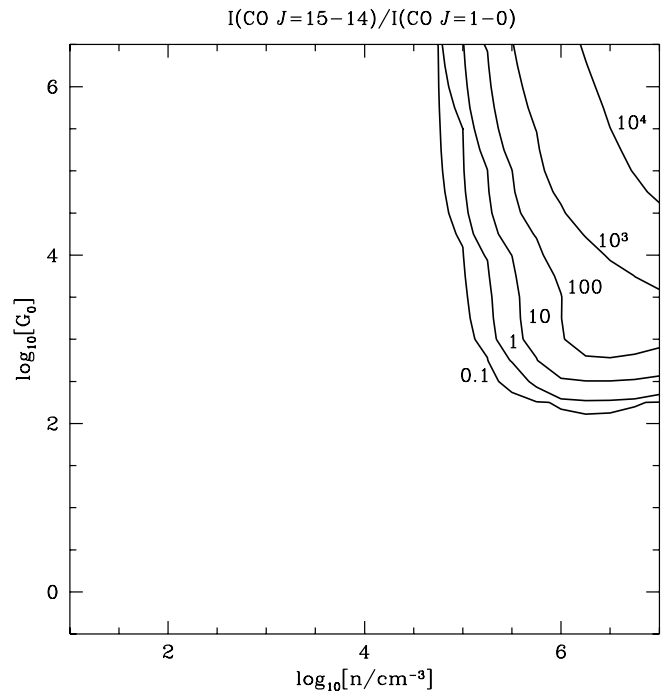
to 10% of their standard values; in addition, the dust abundance, PAH abundance, corresponding visual extinction cross section per H atom, and H_2 formation rate coefficient R_{form} drop to 10% of their standard values. Since our standard PDR models are calculated to a visual extinction of $A_V = 10$, the effect of lowering the dust abundance is to increase the physical extent and total hydrogen column density, N, of a PDR model. A PDR with visual extinction A_V and metallicity Z has a physical size $L = N/n = 2 \times 10^{21} A_V/(Zn)$ cm. Therefore, for a metallicity of $Z = 0.1$ relative to $Z = 1$, we increase the size L by a factor of 10 and the hydrogen column density from 2×10^{22} cm^{-2} to 2×10^{23} cm^{-2} so that the total $A_V = 10$.

In Figures 16, 17, and 18 we show the relative strengths of the CO $J = 1$–0 and [C II] 158 μm lines for models with densities of 10^3 and 10^5 cm^{-3}, for all G_0, and metallicities of $Z = 1.0$ and $Z = 0.1$. Figure 16 shows results for models with total visual extinction $A_V = 10$. Figure 17 has $A_V = 3$, and Figure 18 shows results for $A_V = 1$. In producing these results, we have explicitly calculated the structure of one-dimensional PDR models with lowered metallicity. However, the low A_V results are one-dimensional PDR models truncated at $A_V = 1$ and $A_V = 3$ from the surface. The strengths of the two emission lines are shown relative to the strength of the FIR continuum. We apply a correction to the FIR emission expected from the low-A_V models such that only that portion of the FUV flux that can be absorbed in the reduced column is reemitted as FIR continuum. We again include the factor of 2 bolometric correction to the strength of the FIR field because of illumination outside the FUV band (see § 3.2). Our results illustrate that the effects of metallicity are minor for the parameters of interest. To first order, changing the metallicity by a factor of 10 while keeping A_V constant has little effect since there is an
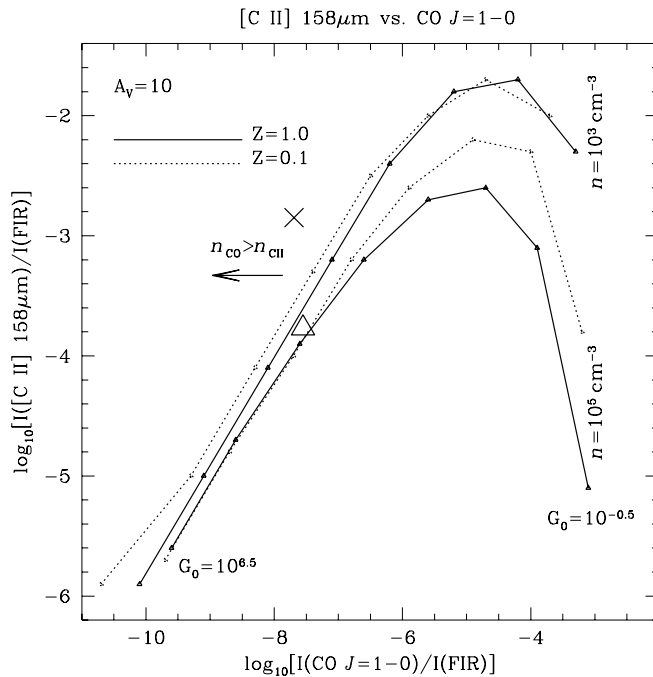
[C II] 158μm vs. CO $J=1-0$

$A_V = 10$

$Z = 1.0$
$Z = 0.1$

$n_{CO} > n_{C II}$

$n = 10^3$ cm^{-3}

$n = 10^5$ cm^{-3}

$G_0 = 10^{-0.5}$

$G_0 = 10^{6.5}$

log$_{10}$[I([C II] 158μm)/I(FIR)]

log$_{10}$[I(CO $J=1-0$)/I(FIR)]

FIG. 16.—Comparison of the [C II] 158 μm and CO $J = 1-0$ transitions scaled relative to the expected FIR intensity, for PDR models with a total slab visual extinction $A_V = 10$. Curves are labeled with density ($n = 10^3$ cm^{-3} and $n = 10^5$ cm^{-3}), and points represent results for different values of the incident FUV radiation field. The rightmost point on each curve is for log $G_0 = -0.5$, with G_0 increasing by a factor of 10 for each step to the left along a curve. The dotted lines $Z = 0.1$ show results for a factor of 10 reduction in the abundance of dust and metals. The arrow indicates the direction of the shift in curves with enhanced density in the CO zone relative to the [C II] zone and for unresolved spherical clouds instead of slab geometry. For $n_{CO} \gg n_{C II}$, the CO luminosity is small compared with L(C II) even for $A_V = 10$, because of the reduced area of the CO photosphere. The arrow also indicates the shift that occurs for spherical clouds of smaller A_V but with $n_{CO} = n_{C II}$. The cross indicates the results for the Large Magellanic Cloud (LMC), and the triangle indicates the results for M82 (see §§ 3.5.2–3.5.3).

[C II] 158μm vs. CO $J=1-0$

$G_0 = 10^{3.5}$

$n = 10^3$ cm^{-3}

$n = 10^5$ cm^{-3}

$G_0 = 10^{4.5}$

$A_V = 3$

$G_0 = 10^{-0.5}$

$Z = 1.0$
$Z = 0.1$

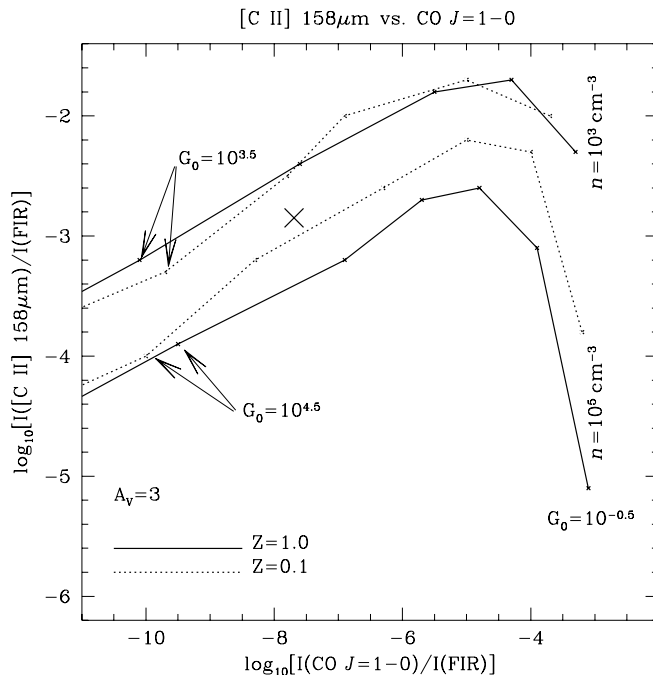log$_{10}$[I([C II] 158μm)/I(FIR)]

log$_{10}$[I(CO $J=1-0$)/I(FIR)]

FIG. 17.—Same as Fig. 16, but for total slab visual extinction $A_V = 3$. Note that very high values of G_0 lie to the far left of the figure. Values for the LMC are again indicated by the cross.

[C II] 158μm vs. CO $J=1-0$

$n = 10^3$ cm^{-3}

$G_0 = 10^{1.5}$

$G_0 = 10^{2.5}$

$A_V = 1.0$

$Z = 1.0$
$Z = 0.1$

$n = 10^5$ cm^{-3}

$G_0 = 10^{-0.5}$

log$_{10}$[I([C II] 158μm)/I(FIR)]
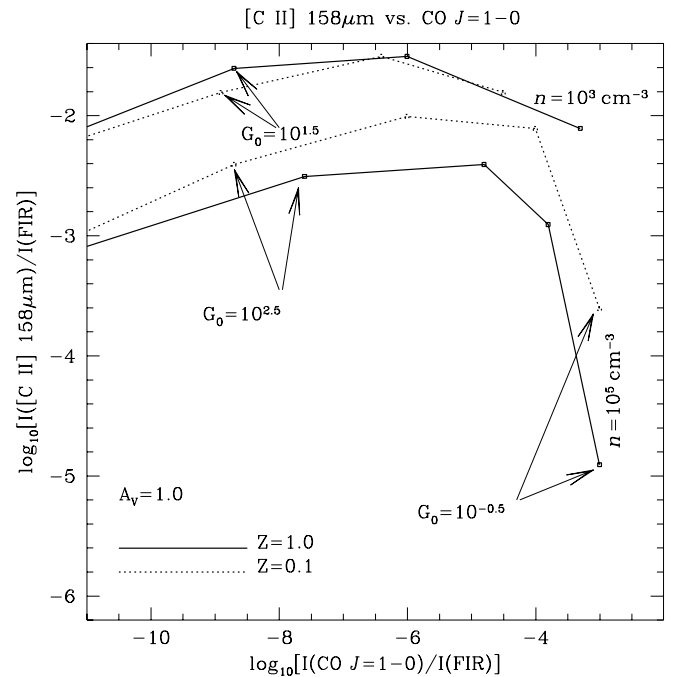
log$_{10}$[I(CO $J=1-0$)/I(FIR)]

FIG. 18.—Same as Fig. 16, but for total slab visual extinction $A_V = 1.0$. Again, very high values of G_0 lie to the far left of the figure. The CO intensity becomes very weak for high values of G_0 because most of the CO is photodissociated and the slab becomes very optically thin in this line.

approximate scaling. Since the species responsible for the heating (small grains) and the species responsible for the cooling (carbon and oxygen) are reduced by the same factor Z, the temperature in the warm PDR zone remains approximately constant while changing Z. In addition, the column of coolant species like O and C$^+$ in the warm zone also remain constant for high $G_0/n \gtrsim 3 \times 10^{-3}$ cm^3, although the H column increases. Therefore, results for models with the same total A_V should be similar.

There are, however, some chemical processes that affect the [C II]/CO ratio as Z is varied. Recall that a prime destruction mechanism for C$^+$ at low G_0/n is by collisions with neutral or negatively charged PAHs. The total PAH abundance as well as the fraction of PAHs that are negatively charged has a Z dependence, with PAH and PAH$^-$ increasing with Z (more gas-phase electrons result in more neutral or negatively charged PAHs). Therefore, the C$^+$ column increases with decreasing Z for $G_0/n \lesssim 10^{-3}$ cm^3. Figures 17 and 18 show this effect, [C II] increasing with decreasing Z, for $n \sim 10^5$ cm^{-3} and $G_0 \lesssim 100$. At lower densities and higher FUV field strengths, dust shielding dominates for both metallicities, the temperature exceeds 92 K so the C$^+$ intensity is insensitive to T, the C$^+$ column is relatively constant, and the curves converge.

For high values of $G_0/n \gtrsim 3 \times 10^{-3}$ cm^3, Figures 17 and 18 show the effect of photodissociation of CO when $A_V = 3$ and $A_V = 1$, respectively. For high values of G_0/n and the relatively low total slab opacity of $A_V = 1$, FUV radiation nearly completely photodissociates the CO throughout the PDR and the CO $J = 1-0$ line becomes optically thin and weak. Carbon is ionized throughout nearly the entire slab. Neither gas shielding nor dust shielding is sufficient to create a C$^+$/C/CO transition. Note that the case of $Z = 0.1$ and $A_V = 1$ presented in Figure 18 corresponds to the same

total column of hydrogen nuclei as the case $Z = 1.0$ and $A_V = 10$ presented in Figure 16. As can be seen by comparing Figures 16, 17, and 18, the [C II]/CO ratio is vastly different for $G_0 \gtrsim 10$, because of the steep decline in the CO intensity for $A_V \ll 10$. Thus, reducing Z in a cloud of given total column density has a dramatic effect, while reducing Z in a cloud of given A_V has much less effect. Note that once $A_V \lesssim 1$ not all of the incident radiation is absorbed by the slab and reradiated, so $I(\text{FIR})$ is reduced compared to higher opacity cases, an effect that we have included in Figures 17 and 18.

In Figure 16, we also indicate the trend in the [C II]/CO ratio for the case of unresolved spherical clouds illuminated from the outside so that the outer layers of the clouds have carbon mostly in C^+, while the central regions contain carbon in CO. The arrow extending to lower CO intensity indicates that for spherical clouds the emitting area of C^+ becomes larger than that of CO. For clouds with visual extinctions to their centers of $A_V = 10$ and constant hydrogen density from the outer C^+ zone to the inner CO core ($n_{C^+} = n_{CO}$), this effect is minor. The $C^+/C/CO$ transition occurs at $A_V \lesssim 3$ into the cloud, and therefore the CO photosphere has almost the same radius as the entire cloud (the C^+ zone can be considered a thin shell on the outside of this spherical cloud). Lowering the total A_V of the cloud, however, tends to move the CO photosphere in toward the center of the cloud, reducing the emitting area of the optically thick CO emission region and enhancing [C II] relative to CO. The same effect occurs if the hydrogen density of the CO core, n_{CO}, is higher than that of the [C II]-emitting region, $n_{C\,II}$: a higher density CO core has a smaller physical size for a given A_V, so [C II]/CO can be enhanced by a large factor by increasing n_{CO} relative to $n_{C\,II}$. The arrow in Figure 16 shows the trend with an increase in the CO core density or a decrease in A_V for spherical clouds. We emphasize that this effect applies to unresolved cores.

3.4.2. The CO/H_2 Ratio in Spherical Clouds

The CO $J = 1-0$ luminosity, $L(\text{CO } J = 1-0)$, is used as a tracer of H_2 mass, M_{H_2}. Here we investigate the effects of total cloud column density N and metallicity Z on the ratio $L(\text{CO } J = 1-0)/M_{H_2}$. As noted in the previous section, the product NZ or the A_V through the cloud has the largest effect on the CO emission from a PDR model. We also probe the sensitivity of $L(\text{CO } J = 1-0)/M_{H_2}$ to variations in G_0 and n. We have made a very simplified calculation of the ratio $L(\text{CO } J = 1-0)/M_{H_2}$ to be expected from spherical clouds by assuming that our one-dimensional slab model results accurately describe the (escaping) volume emissivity $j(N)$ in the $J = 1-0$ line as a function of A_V for a spherical cloud. We have not explicitly calculated spherical models nor have we included an escape probability appropriate for spherical geometry. To find the CO luminosity of a particular cloud we calculate

$$L(\text{CO } J = 1-0) = \int 4\pi j(N) r^2 \, dr , \quad (1)$$

where $r = (N_{\text{total}} - N)/n$ is the radial coordinate and $j(N)$ is the emissivity in the 1–0 line at a column N from the surface computed from our slab models. For example, a cloud with a column density of 2×10^{21} cm^{-2} from the surface to the center has the emissivity calculated for $A_V \sim 0$ at the surface and the emissivity calculated for $A_V = 1$ at the center. We calculate $L(\text{CO } J = 1-0)$ as a function of the column density

to the center of a spherical cloud for columns up to $10^{22.3}$ cm^{-2} for the case of $Z = 1$ and for columns up $10^{23.3}$ cm^{-2} for the case of $Z = 0.1$. For comparison, Störzer, Stutzki, & Sternberg (1996) have explicitly calculated the structure of spherical PDRs; they find that the temperature and chemical profiles of constant density spherical PDRs are very similar to those for plane-parallel PDRs, especially when the column density is high enough that the $C/C^+/CO$ transition occurs near the cloud surface. They do find that this transition occurs nearer the PDR surface for plane-parallel models than for spherical models in low column density cases, an effect that is smaller than 20% for the cases they present. Since the CO line is generally optically thick and is relatively insensitive to temperature, we expect that our simplified calculation will give results within a factor of 1.5 larger than a detailed spherical model.

Our results are shown in Figure 19 for $Z = 1$ and in Figure 20 for $Z = 0.1$. Moving to the right along the x-axis in these figures is equivalent to increasing the total visual extinction (upper x-axis) or total cloud hydrogen column density (lower x-axis) to the center of the spherical cloud. Results are shown for $G_0 = 1$, $10^{1.5}$, and $10^{3.5}$ and for densities $n = 10^2$, 10^3, and 10^4 cm^{-3}. At very low visual extinctions, the ratio is small since the CO is photodissociated more effectively than the H_2. As we move to higher total visual extinction, the ratio $L(\text{CO } J = 1-0)/M_{H_2}$ drops near $A_V \sim 1$ (for high ratios of G_0/n where dust controls the H/H_2 dissociation front) as molecular hydrogen begins to form but CO is still photodissociated. As CO becomes the dominant carbon-bearing species ($A_V \gtrsim 2$), the ratio again begins to rise. In the case of low G_0, the ratio eventually drops as we move to higher total A_V since CO is optically thick near the surface and $L(\text{CO } J = 1-0)$ roughly scales with cloud area (or A_V^2 for fixed n) while M_{H_2} scales with volume (or A_V^3 for fixed n). Therefore the ratio of the two
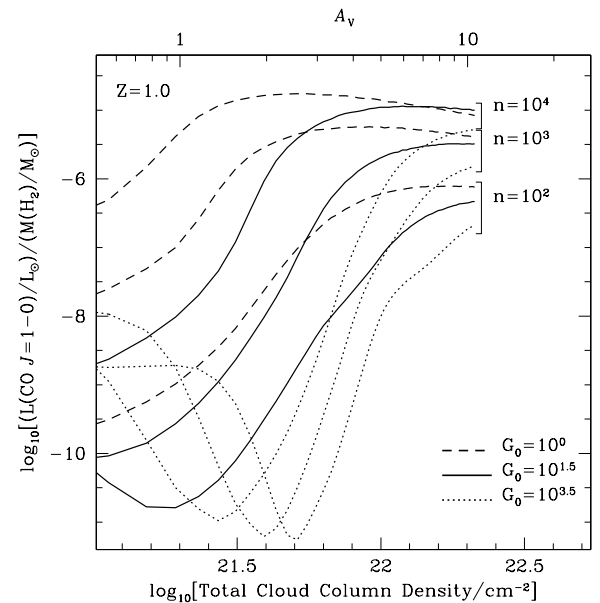

FIG. 19.—CO $J = 1-0$ luminosity (in units of $L_\odot$) divided by total H_2 mass (in units of $M_\odot$) for spherical PDR models with various central optical depths or columns (see text). Results are presented for clouds with densities $n = 10^2$, 10^3, and 10^4 cm^{-3} and for FUV intensities $G_0 = 1$ (dashed curves), $10^{1.5}$ (solid curves), and $10^{3.5}$ (dotted curves). The standard conversion factor corresponds to a value $\sim 8 \times 10^{-6}$ $L_\odot/M_\odot$, or 1.7×10^{-7} K km s^{-1} kpc^2 $M_\odot^{-1}$.
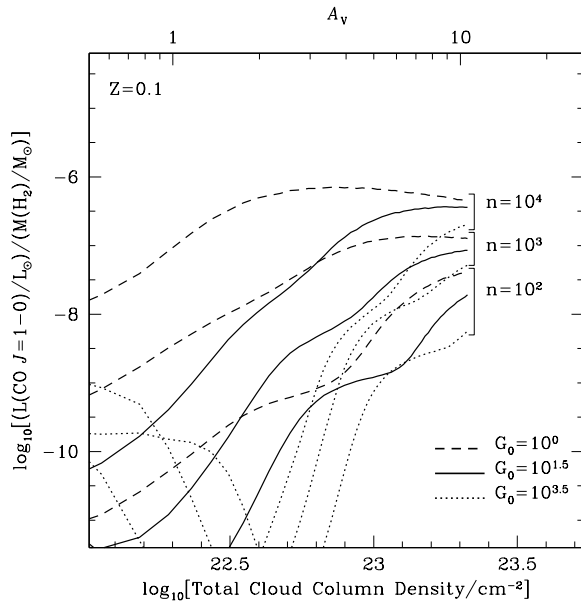
FIG. 20.—Same as Fig. 18, but for $Z = 0.1$. Note the difference in the total cloud column density scale.

declines as A_V (and cloud radius) gets larger. In the case of a very high FUV field ($G_0 \gtrsim 100$), the CO photospheric radius is appreciably smaller than the H_2 radius even when $A_V = 10$. The CO photospheric area therefore increases faster than the H_2 volume, and the ratio continues to rise as A_V increases from 3 to 10. Lowering the metallicity to $Z = 0.1$ but fixing A_V leads to a smaller ratio since the volume (mass) of the molecular gas is increased relative to the area of the CO photosphere (cf. Fig. 20). The ratio is also a strong function of density between $n = 10^2$ cm^{-3} and $n = 10^4$ cm^{-3}, in part because of chemical effects and in part to the fact that the critical density for this transition is $n \sim 3 \times 10^3$ cm^{-3} (cf. Table 2).

The main points illustrated in Figures 19 and 20 are the following. The $L(\mathrm{CO}\ J = 1{-}0)/M_{H_2}$ ratio varies over many orders of magnitude for clouds of low $A_V \lesssim 3$. Even if all clouds have the same (high) value $A_V \approx 10$, there are still order-of-magnitude changes in the ratio as Z and n vary. The drop of ~ 10 in the ratio as Z drops from 1 to 0.1 is primarily due to the increased size of the clouds, which changes the volume ($\sim H_2$ mass) by a factor of 10 more than it changes the CO photospheric area [$\sim L(\mathrm{CO})$]. For $A_V = 10$, a drop in Z from 1 to 0.1 increases the radius of a cloud by a factor of 10, increasing the H_2 mass by a factor of 10^3 but increasing the area of the CO photosphere by only a factor of 10^2. For virialized clouds, as the ratio M/R increases by a factor of 100, the turbulent Doppler velocity δ_{v_D} should also increase by a factor of 10. Wolfire et al. (1989) showed that variations of δ_{v_D} by a factor of 2 had little effect on the line intensities, but this larger increase in velocity dispersion might have a significant effect on the intensity of the CO $J = 1{-}0$ line; we have not included this effect in our models. The $L(\mathrm{CO}\ J = 1{-}0)/M_{H_2}$ ratio also drops by about an order of magnitude for fixed Z as n decreases from 10^4 cm^{-3} to 10^2 cm^{-3}, primarily because of subthermal excitation of CO. However, the ratio is quite insensitive to large variations (over 3 orders of magnitude) in G_0. The standard ratio $L(\mathrm{CO}\ J = 1{-}0)/M_{H_2}$ is typically taken as $\sim 8 \times 10^{-6}\ L_\odot/M_\odot$ (e.g., Young et al. 1986), which

corresponds to $Z = 1$, $A_V = 10$, $n \sim 10^4$ cm^{-3}, and $G_0 \sim 1{-}100$ (cf. Fig. 19).

3.5. Application to Extragalactic Sources

3.5.1. Sources Smaller than the beam

In the previous sections of this paper, we have implicitly assumed that a single PDR is contained within the observer's beam. This is the case, for example, for the Orion PDR behind the Trapezium, where a typical 60″ beam covers ~ 0.15 pc, a size much smaller than the emitting region of ~ 1 pc. In extragalactic observations, however, the physical size of the beam at the distance of the source (typically about a kiloparsec) is large compared with a single PDR, and the observed emission arises from many separate PDR surfaces. In this subsection, we mention several cautionary notes when applying our theoretical models to these types of observations and further outline the additional analysis that can be carried out for extragalactic sources.

First note that the observed line width measures the dispersion velocity of PDRs (clouds) within the beam rather than the turbulent gas velocity, δv_D, within a single PDR. Thus, the appropriate δv_D to use for extragalactic observations is of the order a few km s^{-1} as adopted in this paper, and δv_D is not the much larger velocity width of the emission line.

Second, the observed peak line intensity depends on the intensity emitted by each cloud and the beam filling factor at the central velocity. It is important, therefore, to correct as best as possible for the different area filling factors for various species. For example, diffuse [C II] emission may fill the beam whereas [O I] emission may arise from a smaller, high-n, and high-T region. In such a case it would not be appropriate to take the ratio of observed fluxes $\mathscr{F}([\mathrm{C\ II}])/\mathscr{F}([\mathrm{O\ I}])$ for use in the contour plots presented in this paper. The ratio of intensities $I([\mathrm{C\ II}])/I([\mathrm{O\ I}]) = \mathscr{F}([\mathrm{C\ II}])/\Omega_{[\mathrm{C\ II}]}/\mathscr{F}([\mathrm{O\ I}])/\Omega_{[\mathrm{O\ I}]}$ should be used for the ratio of fluxes corrected for the separate [C II]– and [O I]–emitting solid angles, $\Omega_{[\mathrm{C\ II}]}$ and $\Omega_{[\mathrm{O\ I}]}$. The density, temperature, and incident FUV field derived from the observations are necessarily an ensemble average of the PDRs in the beam. WTH90 analyzed the bias in the derived quantities and found that the method is somewhat biased toward the high-density, high-G_0 regions.

A third caution is that some portion of the diagnostic line emission, in particular that of [C II], may arise from non-PDR gas such as that from low-density H II regions or a diffuse warm ionized component. This emission should be subtracted before using the contour plots. One method for estimating this emission is to rely on H II region modeling as presented, for example, in Carral et al. (1994), or from CLOUDY (Ferland 1996) models. Carral et al. estimated that 30% of the [C II] emission in NGC 253 originates in H II regions. Another method may be used when [N II] emission is observed, as the [C II] emission from low-density H II regions scales with [N II] (Heiles 1994).

Having obtained the average density n, temperature T, and incident FUV field G_0, from the far-infrared line and continuum observations, the analysis explained in WTH90 and Carral et al. (1994) can be carried out to determine additional characteristics of the interstellar medium. The first step is to determine the mass of neutral PDR gas from the observed [C II] line intensity and the derived gas temperature and density from observations of [C II], [O I] and

the FIR continuum flux from the warm dust in the PDRs. If CO observations are available, then estimates can be made of the molecular gas mass, the area and volume filling factor of the clouds, and the number and radii of clouds. The last step is to evaluate the source of FUV radiation as being consistent with a distribution of stars or a central source and whether the absorbing clouds are correlated in space with the FUV source(s).

We will not repeat the steps here, and the reader should refer to the original papers for details; however, a few points should be noted in applying the updated models. Note that the [C II] cooling plot shown in WTH90 (Fig. 4) is acceptable for use with the current models with the reduced gas-phase carbon abundance. This is because the plot shows the cooling per C^+ atom as opposed to the cooling per hydrogen nucleus, and thus it remains unchanged for present models. Also note that only the surface temperature is presented in this paper, while both a surface temperature and maximum temperature were shown in WTH90. With the updated PAH heating we find that the maximum temperature is at, or close to, the surface and we can take T_S to be the characteristic PDR temperature. The remaining analysis should proceed unchanged from the former papers.

3.5.2. *Application to M82*

Our model results may be used to determine a variety of parameters of the ISM in external galaxies. In order to compare our results with those of WTH90, we have repeated the analysis of the conditions in the starburst galaxy M82 using the data from Lord et al. (1996a), who measured the strength of the [O I] 63 μm line from the central regions of M82 and compared it with the strengths of the [C II] 158 μm line measured by Stacey et al. (1991), the [O I] 145 μm line measured by Lugten et al. (1986) and the FIR continuum emission measured by Telesco & Harper (1980). The measured fluxes in the [O I] 63 μm, [O I] 145 μm, and [C II] 158 μm lines and the FIR continuum are 1.31×10^{-10}, 0.84×10^{-11}, 1.42×10^{-10}, and 9.3×10^{-8} ergs cm^{-2} s^{-1}, respectively. The [C II] emission from M82 emerges from a far more extended region than the [O I] emission and was measured with a larger beam, so we have compared the line ratios in two limits. At a distance of 3.25 Mpc, the [C II] and [O I] beam sizes are ~ 1 kpc and 400×200 pc, respectively, so we are studying gas in the very central regions of M82.

In the first case, we assume that the [C II] emission has equal intensity over the entire [C II] beam, so that the [C II] flux emerging from the [O I] emitting region is just the [C II] flux reduced by the ratio $\Omega_{[O I]}/\Omega_{[C II]} \sim 0.112$, where $\Omega_{[O I]}$ and $\Omega_{[C II]}$ are the beam solid angles of emission in each of the lines. This gives a [C II] flux from the [O I] emitting region of 1.59×10^{-11} ergs cm^{-2} s^{-1}. The resultant ratios are $F[O I]$ 63 μm/$F[C II]$ 158 μm = 8.24, $F[O I]$ 145 μm/$F[O I]$ 63 μm = 0.064, and $(F[O I]$ 145 μm + $F[C II]$ 158 μm)/F(FIR) = 1.58×10^{-3} (which we divide by 2 for an extragalactic source, as described in § 3.2). Comparing the first two line ratios and overlaying Figures 4 and 5, we find typical conditions of $n = 10^4$ cm^{-3} and $G_0 = 10^{3.5}$; by comparing $F[O I]$ 63 μm/$F[C II]$ 158 μm with the line-to-continuum ratio, and using Figures 4 and 6, we find $n = 10^{3.9}$ cm^{-3} and $G_0 = 10^{3.4}$. As an additional check on this procedure, we can compare the ratio of the two neutral carbon transitions (Fig. 8), $I([C I]$ 370 μm)/$I([C I]$ 609 μm) = 4.3 (Stutzki et al. 1997) with the far-infrared line-to-

continuum ratio and again find $n \sim 10^4$ cm^{-3}, $G_0 \sim 10^4$. For the purposes of the following discussion, then, we take $n = 10^4$ cm^{-3} and $G_0 = 10^{3.5}$ as representative conditions in the central region of M82. Reference to Figure 1 indicates a surface temperature $T_S \sim 400$ K. These values of T_S, n, and G_0 are somewhat different than those calculated by Lord et al. for the central regions of M82—$T_S = 230$ K, $n = 10^{3.9}$ cm^{-3}, and $G_0 = 10^{3.0}$—because of the changes in our PDR model as described above.

Following the procedure outlined in WTH90, we can estimate the mass of the neutral PDR gas from the observed [C II] flux from the [O I]–emitting region. To facilitate our comparison with the results of Lord et al. (1996a), we use a distance of 3.25 Mpc to M82, but we use a revised elemental C abundance of 1.4×10^{-4}. Using Figure 4 of WTH90 and a surface temperature $T_S = 400$ K, we find a cooling power of 1.1×10^{-21} ergs s^{-1} cm^{-2} sr^{-1} per C^+ atom; then equation (2) of WTH90 gives an atomic gas mass of $M_a = 8.83 \times 10^6$ $M_\odot$. We can compare this to the total molecular mass $M_m \sim 2 \times 10^8$ $M_\odot$ as determined by observations of optically thick CO $J = 1-0$ emission (Wild et al. 1992).

Following the method of WTH90, we find an area filling factor of clouds $\Phi_A = 2.7$ by taking the ratio of the observed [C II] intensity to the predicted intensity as given by Figure 3 for $n = 10^4$ cm^{-3} and $G_0 = 10^{3.5}$. For comparison, the same procedure, when applied to the [C I] 609 μm and CO $J = 1-0$ lines, where $I([C I]$ 609 μm) and $I(CO J = 1-0)$ equal $\sim 10^{-5}$ and $\sim 2 \times 10^{-7}$ ergs cm^{-2} s^{-1} sr^{-1}, respectively (e.g., Stacey et al. 1993; White et al. 1994), also yields filling factors of ~ 2, according to Figures 7 and 11. As discussed by WTH90, for clouds illuminated by an FUV radiation field over 4π sr, the projected cloud area filling factor $\Phi'_A = \Phi_A/4 = 0.67$. Using the molecular mass estimate and assuming a molecular-to-atomic gas density ratio $\eta = 3$, we derive a volume filling factor $\Phi_V = 6.2 \times 10^{-3}$ (eq. [12] of WTH90). With these parameters, we may calculate the following average cloud properties for the central regions of M82: cloud radius $r_{cl} = 1.7$ pc, number of clouds $N_{cl} \sim 7500$, and a mean free path between clouds $\lambda = 365$ pc, assuming a spherical distribution. Our results imply cloud masses $M_{cl} \sim 3 \times 10^4$ $M_\odot$, somewhat smaller than massive giant molecular clouds (GMCs) in the Galaxy. However, these clouds have thermal pressures of order ~ 100 times those of GMCs, resulting from a factor ~ 10 higher temperature and from a factor ~ 10 higher n.

For comparison, we have repeated the above calculation assuming that all of the [C II] emission from M82 arises from the same gas that is responsible for the [O I] emission (i.e., a much lower [O I]/[C II] ratio). Using the same procedure, we derive the following average properties: $n \sim 10^{2.7}$, $G_0 \sim 10^{2.5}$, $M_a \sim 4 \times 10^8$ $M_\odot$, $\Phi_A \sim 50$, $r_{cl} \sim 23$ pc, $N_{cl} \sim 770$, and $M_{cl} \sim 1.2 \times 10^6$ $M_\odot$. This large variation in our results for cloud masses, numbers of clouds, etc., determined above shows the sensitivity of our results to the assumed details of the emitting region. Therefore, independent measures that can further constrain the conditions in M82 (e.g., SOFIA observations of the spatial extent of the CII–emitting region region) will decrease the range of possible conditions determined from these models. In the absence of other independent measurements, these models can show trends in n, T, pressure, and UV field for a large statistical sample of galaxies. These trends might be compared, e.g., with star formation activity or the presence of active galactic nuclei (AGNs). Our method is more useful

for comparing galaxies than for determining absolute numbers for these properties.

3.5.3. *Application to NGC 278*

As a second application of our results, we use a similar method to determine the average properties of the interstellar medium in the spiral galaxy NGC 278.[2] NGC 278 was observed in a number of lines including [C II] 158 μm, [O I] 63 and 145 μm, and [N II] 122 μm, with fluxes of 0.69, 0.31, 0.013, and 0.030 $\times 10^{-18}$ W cm^{-2}, respectively. The measurement of the strength of the [N II] line, which arises from ionized gas, gives us an independent measure of the contribution of H II regions to the [C II] line flux. From theoretical considerations, Heiles (1994) concludes that the [C II] flux from H II regions is ~ 6.5 times that of [N II] 122 μm, assuming an H II region temperature of 10^4 K and our standard carbon abundance (see Table 1). Measurements from the *COBE* satellite (Wright et al. 1991; Petuchowski & Bennett 1993) show this ratio is ~ 8.7 for Galactic H II regions. Thus we expect that 7–8 times the [N II] flux emerges from H II regions as [C II] flux. Applying this correction, we find that the [C II] flux from PDR gas in NGC 278 is $\simeq 0.44 \times 10^{-18}$ W cm^{-2}, assuming NGC 278 has the same C/N ratio as the Milky Way. *IRAS* measurements of the 60 and 100 μm flux from NGC 278 (Moshir et al. 1990) translate to a FIR flux of $\sim 1.34 \times 10^{-16}$ W cm^{-2}.

For the measured PDR line strengths, we find [O I] 63 μm/[C II] 158 μm, [O I] 145 μm/[O I] 63 μm, and ([O I] 63 μm + [C II] 158 μm)/FIR ratios of 0.69, 0.042, and 5.6×10^{-3}, respectively. Using Figures 4, 5, and 6 we may estimate the average properties of the ISM in NGC 278. From the pair of line ratios, we find $n \sim 5 \times 10^3$ cm^{-3} and $G_0 \sim 30$. From the [O I]/[C II] ratio and the line to continuum ratio (including the factor of 2 correction when using Figure 6 for extragalactic sources) we find $n \sim 10^3$ cm^{-3} and somewhat higher $G_0 \sim 140$. As mean properties, then, we assume $n = 2 \times 10^3$ cm^{-3} and $G_0 = 70$. We find lower values of G_0 and n for this galaxy than the values for M82. This is expected since NGC 278 is a "normal" galaxy compared with the starburst nucleus of M82. Since NGC 278 lies at a distance of 12.4 Mpc (Braine et al. 1993), the observations are sampling nearly 4 kpc of the disk of NGC 278, as opposed to roughly 1 kpc of the M82 disk, so the sampled regions represent a more global average than those of the central regions of M82.

With these average properties, we have repeated the WTH90 process for determining typical parameters of the ISM in NGC 278. From Figure 1, we estimate a surface temperature $T_S \sim 200$ K, which leads to an estimate of the mass of atomic gas from PDRs, $M_a \sim 5 \times 10^7$ $M_\odot$, more than 5 times larger than in M82. This can be compared with the estimated mass of molecular gas, $M_m \sim 1.7 \times 10^9$ $M_\odot$ (Young et al. 1996). Following the WTH90 method, we find an area filling factor of clouds $\Phi_A = 0.35$. Using the same estimate of the molecular-to-atomic gas density ratio, $\eta = 3$, we find the number of molecular clouds, $N_{cl} \sim 3 \times 10^4$, cloud radii, $r_{cl} \sim 5.5$ pc, and cloud mass, $M_{cl} \sim 3.5 \times 10^4$ $M_\odot$. Assuming the GMCs are confined to a galactic disk with thickness ~ 200 pc, we find a volume filling factor in the disk of $\simeq 3.5 \times 10^{-3}$ and a mean free path between

clouds in the disk of ~ 1 kpc. We note that, compared with our first model of M82, the clouds have similar mass and size. The mean free path between clouds is also similar, although the clouds in M82 are a bit smaller in size and closer together as might be expected. However, the clouds in M82 have much greater incident FUV fluxes and are at much higher thermal pressures. This, too, is not entirely unexpected.

3.5.4. *Application to the LMC*

As an application of the model results presented in Figures 16–20, we compare the [C II]/FIR and CO/FIR ratios for the LMC. Poglitsch et al. (1995) observed 30 Doradus in the LMC with a 1′ beam (~ 15 pc at the LMC) and found [C II] 158 μm, CO $J = 1-0$, and FIR continuum intensities of 1×10^{-3}, 1.4×10^{-8}, and 0.7 ergs s^{-1} cm^{-2} sr^{-1}, respectively. These results give I[C II]/I(FIR) $= 1.4 \times 10^{-3}$ and I[CO]/I(FIR) $= 2.0 \times 10^{-8}$. These values are indicated with a large cross in Figures 16 and 17. The figures show that the observations may be matched either by high extinction ($A_V = 10$) clouds with moderate densities and FUV fields ($G_0 \sim 10^3$) but with $n_{CO} > n_{C II}$ so that the area of CO emitting gas is effectively decreased relative to the area of [C II] emitting gas; or by lower extinction ($A_V \sim 3$) gas illuminated with $G_0 \sim 300$ with equal densities ($n \sim 10^4$ cm^{-3}) in the CO- and [C II]–emitting regions, which again tends to lower the ratio of CO-to-[C II] emitting areas.

If the CO- and [C II]–emitting regions have the same density, then our results from Figure 17 allow us to constrain the implied value of the ratio L(CO $J = 1-0$)/M_{H_2}. For low metallicity, $n \sim 10^4$ cm^{-3} and $G_0 \sim 300$, and, taking $A_V \sim 3$, Figure 20 shows that the ratio has a value of $\sim 3 \times 10^{-9}$, a factor of $\sim 2 \times 10^3$ smaller than the standard ratio. This low ratio implies that the mass of clouds in the LMC is larger by this factor than the standard ratio would give. Using this conversion factor, we can calculate the mass of H$_2$ in the 1′ beam from the observed CO intensity. If we assume that typical GMCs are ~ 15 pc in size, then the 1′ beam contains a single GMC. We find a mass $M_{H_2} \sim 2.5 \times 10^7$ $M_\odot$, more than an order of magnitude too high for a 15 pc cloud to be gravitationally stable. This seems to rule out our $A_V = 3$ model, so we conclude that the $A_V = 10$ model with a density contrast between the CO- and [C II]–emitting regions is far more likely. The $A_V = 10$ model is consistent with the McKee (1989) model of photoionization regulated star formation, which predicts that A_V remains constant even as Z changes.

4. SUMMARY

We have modeled the emission from photodissociation regions using the PDR code of TH85, but updated through the use of the most up to date values of atomic and molecular data, chemical rate coefficients, and grain photoelectric heating rates. We find that the new grain heating terms produce the largest differences between our results and earlier results of our group. We have presented contour plots showing the line intensity and/or intensity ratios for the PDR diagnostic lines [C II] 158 μm, [O I] 63 μm and 145 μm, [C I] 370 μm and 609 μm, CO $J = 1-0$, $J = 2-1$, $J = 3-2$, $J = 6-5$, and $J = 15-14$, as well as the strength of the FIR continuum. The contour plots cover a large range of density and incident FUV flux, including conditions relevant to diffuse Galactic PDR emission, the surfaces of

---

[2] These data were obtained with *ISO* under the NASA Key Project on Normal Galaxies (Helou et al. 1996) and will appear in S. Malhotra et al. (1999, in preparation).

GMCs exposed to the average interstellar field, planetary nebulae, reflection nebulae, and PDRs lying outside dense H II regions around O and B stars. These plots can be used to derive the gas density n, incident FUV flux G_0, and gas temperature T in PDR regions from observations of line fluxes.

We have explored the effects of metallicity, cloud geometry and visual extinction on the [C II]/FIR and CO $J = 1$–0/FIR intensity ratios. We find that reducing the metallicity in a cloud of fixed A_V (~ 10) has little effect on the [C II]/CO line ratio except in the parameter regime $G_0/n < 3 \times 10^{-3}$ cm^3, where the [C II]/CO ratio increases with decreasing Z (see Fig. 16). For translucent clouds ($A_V \sim 1$–3) changes in metallicity have a more pronounced effect than in the $A_V \sim 10$ case (see Figs. 17 and 18). We find that reducing the A_V of a cloud greatly increases the observed [C II]/CO line ratio. Therefore, reducing the metallicity in a cloud of given total hydrogen column density increases this ratio. Increasing the density of the CO-emitting gas relative to that of the [C II]–emitting gas in an unresolved spherical cloud produces an increase in this ratio as well, because the area of the CO photosphere (and consequently the CO luminosity) is reduced.

We have applied our results to recent observations of the central ~ 500 pc of the starburst galaxy M82. Using the cloud ensemble technique from WTH90 together with our new model results, we find that the core of M82 contains clouds with the following average properties: gas density, $n \sim 10^4$ cm^{-3}; FUV flux, $G_0 = 10^{3.5}$; surface temperature, $T_S = 400$ K; total mass of atomic gas in all the cloud surfaces, $M_a \sim 8.8 \times 10^6$ $M_\odot$; number of molecular clouds, $N_{cl} \sim 7500$; cloud mass, $M_{cl} \sim 3 \times 10^4$ $M_\odot$; and cloud radii, $r_{cl} \sim 1.7$ pc. These clouds have masses akin to GMCs in the Galaxy, though they are denser and at pressures of order 100–1000 times that of local GMCs. Our derived values for the gas densities of these clouds and the mean incident FUV flux are similar to previously determined values. On the other hand, for emission over ~ 4 kpc of the spiral galaxy NGC 278, we find typical values of $n \sim 2 \times 10^3$ cm^{-3}, $G_0 = 70$, $T_S = 200$ K, $M_a \sim 5 \times 10^7$ $M_\odot$, $N_{cl} \sim 3 \times 10^4$, $M_{cl} \sim 3.5 \times 10^4$ $M_\odot$, and $r_{cl} \sim 5.5$ pc. The lower values of n and G_0 are expected since we are averaging over a greater volume of the galaxy and because NGC 278 is not a starburst galaxy like M82. We find that the recently observed high [C II]/CO ratio in the 30 Doradus region of the LMC can be explained by either a lower A_V ($A_V \sim 3$) in the typical clouds compared with clouds in the Milky Way Galaxy ($A_V \sim 10$), or by a higher density in the CO-emitting cloud cores compared with the [C II] halos. In either case, the column of hydrogen nuclei through the typical clouds is greater than the columns through Milky Way molecular clouds. If the [C II]/CO ratio in 30 Doradus is caused by $A_V \sim 3$ clouds, then the CO-to-H$_2$ conversion factor for these clouds is reduced by a factor of as much as $\sim 10^3$ compared to Milky Way clouds. This ratio gives an H$_2$ mass for GMCs in the LMC an order of magnitude too high for the clouds to be gravitationally stable, so we rule out low-A_V clouds as an explanation for the high [C II]/CO ratio. Instead, we find it more likely that these GMCs have $A_V = 10$, consistent with the McKee (1989) model of photoionization regulated star formation, which predicts that A_V remains constant even as Z changes.

REFERENCES

Abgrall, H., Le Bourlot, J., Pineau des Forêts, G., Roueff, E., Flower, D. R., & Heck, L. 1992, A&A, 253, 525
Bakes, E. L. O., & Tielens, A. G. G. M. 1994, ApJ, 427, 822
———. 1998, ApJ, 499, 258
Blum, R. D., & Pradhan, A. K. 1992, ApJS, 80, 425
Braine, J., Combes, F., Casoli, F., Dupraz, C., Gerin, M., Klein, U., Wieblinski, R., & Brouillet, N. 1993, A&AS, 97, 887
Burton, M., Hollenbach, D. J., & Tielens, A. G. G. M. 1990, ApJ, 365, 620
———. 1992, ApJ, 399, 563
Büttgenbach, T. H., Keene, J., Phillips, T. G., & Walker, C. K. 1992, ApJ, 397, L15
Carral, P., Hollenbach, D. J., Lord, S. D., Colgan, S. W. J., Haas, M. R., Rubin, R. H., & Erickson, E. F. 1994, ApJ, 423, 223
Dalgarno, A., & McCray, R. A. 1972, ARA&A, 10, 375
Dixon, W. V. D., Hurwitz, M., & Bowyer, S. 1998, ApJ, 492, 569
Draine, B. T., & Bertoldi, F. 1996, ApJ, 268, 269
Draine, B. T., Roberge, W. G., & Dalgarno, A. 1983, ApJ, 264, 485
Draine, B. T., & Sutin, B. 1987, ApJ, 320, 803
Ferland, G. J. 1996, Internal Report, Univ. Kentucky Dept. Phys. and Astron.
Fischer, J., et al. 1996, A&A, 315, L97
Heiles, C. 1994, ApJ, 436, 720
Helou, G., et al. 1996, BAAS, 189, 6704
Hollenbach, D., & McKee, C. F. 1979, ApJS, 41, 555
———. 1989, ApJ, 342, 306
Hollenbach, D., Takahashi, T., & Tielens, A. G. G. M. 1991, ApJ, 377, 192 (HTT91)
Hollenbach, D., & Tielens, A. G. G. M. 1997, ARA&A, 35, 179
———. 1999, Rev. Mod. Phys., 71, 173
Israel, F. P., Maloney, P. R., Geis, N., Herrmann, F., Madden, S. C., Poglitsch, A., & Stacey, G. J. 1996, ApJ, 465, 738
Jaquet, R. Staemmler, V., Smith, M. D., & Flower, D. R. 1992, J. Phys. B, 25, 285
Jura, M. 1974, ApJ, 191, 375
Köster, B., Störzer, H., Stutzki, J., & Sternberg, A. 1994, A&A, 284, 545

Le Bourlot, J. G., Pineau des Forêts, G., Roueff, E., Dalgarno, A., & Gredel, R. 1993, ApJ, 449, 178
Lequeux, J., Le Bourlot, J., Pineau des Fôrets, G., Roueff, E., Boulanger, F., & Rubio, M. 1994, A&A, 292, 371
Lord, S. D., Hollenbach, D. J., Haas, M. R., Rubin, R. H., Colgan, S. W. J., & Erickson, E. F. 1996a, ApJ, 465, 703
Lord, S. D., et al. 1996b, A&A, 315, L117
Lugten, J. B., Watson, D. M., Crawford, M. K., & Genzel, R. 1986, ApJ, 311, L51
Luhman, M. L., Fischer, J. J., Satyapal, S., Wolfire, M. G., Stacey, G. J., Lord, S. D., Unger, S. J., & Smith, H. A. 1997a, in Extragalactic Astronomy in the Infrared, ed. G. A. Mamon, T. X. Thuan, & J. T. Thanh Van (Paris: Editions Frontières), 149
Luhman, M. L., Jaffe, D. T., Sternberg, A., Herrmann, F., & Poglitsch, A. 1997b, ApJ, 482, 298
Luhman, M. L., et al. 1998, ApJ, 504, L11
Madden, S. C., Geis, N., Genzel, R., Herrmann, F., Jackson, J., Poglitsch, A., Stacey, G. J., & Townes, C. H. 1993, ApJ, 407, 579
Madden, S. C., Poglitsch, A., Geis, N., Stacey, G. J., & Townes, C. H. 1997, ApJ, 483, 200
Malhotra, S., et al. 1997, ApJ, 491, 27
Maloney, P., & Black, J. H. 1988, ApJ, 325, 389
Maloney, P., & Wolfire, M. 1997, in Proc. IAU Symp. 170, CO: Twenty-Five Years of Millimeter-Wave Spectroscopy, ed. W. B. Latter, S. J. E. Radford, P. R. Jewell, J. G. Mangum, & J. Bally (Dordrecht: Kluwer), 299
Mathis, J. S., Rumpl, W., & Nordsieck, K. H. 1977, ApJ, 217, 425
McKee, C. F. 1989, ApJ, 345, 782
McKee, C. F., & Ostriker, J. P. 1977, ApJ, 218, 148
Millar, T. J., Farquhar, P. R. A., & Willacy, K. 1997, A&AS, 121, 139
Moshir, M., et al. 1992, Explanatory Supplement to the *IRAS* Faint Source Catalog, version 2 (SPL D-10015 8/92; Pasadena: JPL)
Pak, S., Jaffe, D. T., van Dishoeck, E. F., Johansson, L. E. B., & Booth, R. S. 1998, ApJ, 498, 735
Péquignot, D. 1990, A&A, 231, 499

Petuchowski, S. J., & Bennett, C. L. 1993, ApJ, 405, 591

Poglitsch, A., Krabbe, A., Madden, S. C., Nikola, T., Geis, N., Johansson, L. E. B., Stacey, G. J., & Sternberg, A. 1995, ApJ, 454, 293

Rothman, L. S., et al. 1987, Appl. Opt., 26, 4078

Sakamoto, S. 1996, ApJ, 462, 215

Satyapal, S., Watson, D. M., Pipher, W. J., Forrest, J. L., Fischer, J., Greenhouse, M. A., Smith, H. A., & Woodward, C. E. 1999, ApJ, 516, 704

Savage, B. D., & Sembach, K. R. 1996, ARA&A, 34, 279

Schröder, K., Staemmler, V., Smith, M. D., Flower, D. R., & Jaquet, R. 1991, J. Phys. B, 24, 2487

Shull, J. M., & Van Steenberg, M. E. 1985, ApJ, 298, 268

Spaans, M., Tielens, A. G. G. M., van Dishoeck, E. F., & Bakes, E. L. O. 1994, ApJ, 437, 270

Stacey, G. J., Geis, N., Genzel, R., Lugten, J. B., Poglitsch, A., Sternberg, A., & Townes, C. H. 1991, ApJ, 373, 423

Stark, A. A., Bolatto, A. D., Chamberlin, R. A., Lane, A. P., Bania, T. M., Jackson, J. M., & Lo, K.-Y. 1997, ApJ, 480, L59

Sternberg, A., & Dalgarno, A. 1989, ApJ, 338, 197

———. 1995, ApJS, 99, 565

Störzer, H., Stutzki, J., & Sternberg, A. 1996, A&A, 310, 592

Stutzki, J., et al. 1997, ApJ, 477, L33

Telesco, C. M., & Harper, D. A. 1980, ApJ, 235, 392

Tielens, A. G. G. M., & Hollenbach, D. J. 1985a, ApJ, 291, 722 (TH85)

Tielens, A. G. G. M., & Hollenbach, D. J. 1985b, Icarus, 61, 40

van Dishoeck, E. F., & Black, J. H. 1986, ApJS, 62, 109

———. 1988a, in Molecular Clouds in the Milky Way and External Galaxies, ed. R. L. Dickman, R. L. Snell, & J. S. Young (Berlin: Springer), 168

———. 1988b, ApJ, 334, 771

Viscuso, P. J., & Chernoff, D. F. 1988, ApJ, 327, 364

White, G. J., Ellison, B., Claude, S., Dent, W. R. F., & Matheson, D. N. 1994, A&A, 284, L23

Wild, W., Harris, A. I., Eckart, A., Genzel, R., Graf, U. U., Jackson, J., Russell, A. P. G., & Stutzki, J. 1992, A&A, 265, 447

Wolfire, M., Hollenbach, D. J., & Tielens, A. G. G. M. 1989, ApJ, 344, 770

———. 1993, ApJ, 402, 195

Wolfire, M., Tielens, A. G. G. M., & Hollenbach, D. 1990, ApJ, 358, 116 (WTH90)

Wolfire, M. G., Hollenbach, D., McKee, C. F., Tielens, A. G. G. M., & Bakes, E. L. O. 1995, ApJ, 443, 152

Wright, E. L., et al. 1991, ApJ, 381, 200

Young, J. S., Allen, L., Kenney, J. D. P., Lesser, A., & Rownd, B. 1996, AJ, 112, 1903

Young, J. S., Kenney, J. D., Tacconi, L., Claussen, M. J., Huang, Y.-L., Tacconi-Garman, L., Xie, S., & Schloerb, F. P. 1986, ApJ, 311, L17